Investigation of the F117A Vortical Flow Characteristics

by

Sabine Anne Vermeersch

B.S. University of Michigan (1991)

SUBMITTED TO THE DEPARTMENT OF
AERONAUTICS AND ASTRONAUTICS
IN PARTIAL FULFILLMENT OF THE REQUIREMENTS
FOR THE DEGREE OF

Master of Science
at the
Massachusetts Institute of Technology

May 1993

Signature of Author _____
Department of Aeronautics and Astronautics
May 6, 1993

Certified by _____
Professor Earll Murman
Thesis Supervisor, Head, Department of Aeronautics and Astronautics

Accepted by _____
Professor Harold Y. Wachman
Chairman, Department Graduate Committee

Investigation of the F117A Vortical Flow Characteristics

by

Sabine Anne Vermeersch

Submitted to the Department of Aeronautics and Astronautics

on May 7, 1993

in partial fulfillment of the requirements for the degree of

Master of Science in Aeronautics and Astronautics

The investigation of the vortical flow around the F117A Stealth Fighter is presented in order to demonstrate the capability to resolve leading edge vortices with an adaptive finite element solver for the Euler equations. The major goal is to capture vortex breakdown at high angles of attack. This work presents the five main steps involved in a typical study of the flow characteristics of a complete aircraft : the definition of the model geometry, the realization of a suitable grid around the discretized model, the implementation of a flow solver, the subsequent analysis of the flow field and the comparison to experimental data sets. The computational data are compared to the lift curves of the aircraft obtained in a subsonic $5' \times 7'$ wind tunnel. The occurance and location of vortex breakdown is determined by performing flow visualization in the tunnel. Five cases are computed for this work. Each case is studied at Mach 0.3 and angles of attack range between 7 and 30 degrees.

Thesis Supervisor: Earll Murman,

Head of Department Aeronautics and Astronautics

Acknowledgments

There are not enough words to thank the many precious people who have shown support during my time at MIT. Many have contributed directly to this work, and others have shared their friendship with me. I will not forget.

First, sincere thanks go to my thesis advisor Earll Murman, for giving me the chance to work with him. It is his enthusiasm, insightful remarks and sincere encouragement that have brought me one step closer to my goals. He has given me enough confidence to last a lifetime. I am also indebted to Professor Jaime Peraire, for spending time on this project during his short visits to MIT; to Joaquim Peiro for all his helpful suggestions; to Bob Haimes for his invaluable assistance and for being at the lab at 7am when the color printer is not working on the day of the deadline and to my student Ioannis Harizopoulos for the wonderful work he did.

I would also like to mention some of the CFD gang : Dave1 for always being patient; Dave2 for sharing his incredible knowledge ; Helene for being such a supportive office-mate ; and Phil, Bilal and Brian for their good company-always. Thanks are also due to some of my special friends : to Linda for keeping me smile with her spontaneity ; to Michael for surprising me so often with impromptu e-mail; to Andras for all the good advice ; and to Aurelie, Pam and Koen, it was a joy to spend time with all of you.

Mostly, there are some people in my life without whom all this would have been impossible. Thanks to K.C., for always being by my side eventhough we were separated. With you, I feel like I am on top of the world ; to my dear parents, for their incredible love and concern for me ; to my sister Rozemarie , I think our friendship is truly unique and to my brother Kristof, for believing that I will never fail.

This research work was partially supported by AFOSR Grant 89-0395, Monitored by Dr. L. Sakell; by McDonnell Aircraft Company, under MDC/MDRL IRAD Sponsorship; by the Zackhartchenko Fellowship; by the Zonta Fellowship; and by the Department of Aeronautics and Astronautics at MIT.

Contents

List of Figures

Chapter 1
Introduction

During the last few years, Computational Fluid Dynamics (CFD) has become a very important tool in predicting fluid flows over bodies. Recent advances in CFD have made it feasible to perform calculations of the flow around complete aircraft configurations. The use of unstructured meshes and grid adaptation are two examples of powerful new approaches. This work was done in order to demonstrate that an adaptive finite element solver on an unstructured mesh of tetrahedra accurately captures and resolves leading edge vortices at high angles of attack. Computations of the inviscid flow field around Lockheed's F117A stealth fighter are performed. This study consists of accurately capturing vortices for the sharp leading edges of the F117A, observing vortex breakdown and determining lift and moment curves for a range of angles of attack. The effects of computational accuracy in relation to grid adaptation and vortex breakdown will also be analyzed. The results are compared to data from wind tunnel experiments to understand their accuracy.

1.1 Background

1.1.1 F117 Stealth Fighter

The main reason for choosing Lockheed's F117A stealth fighter for this project is because of the unusual shape of the aircraft. The design is such that it is optimized to minimize the radar visibility, i.e. create the smallest Radar Cross Section (RCS). Since most aircraft have not been designed for low visibility, the F117A engineers were motivated to consider an unconventional aircraft configuration to achieve the low RCS requirement. The price paid for low RCS can be seen from its unusual shape [11] : a body made

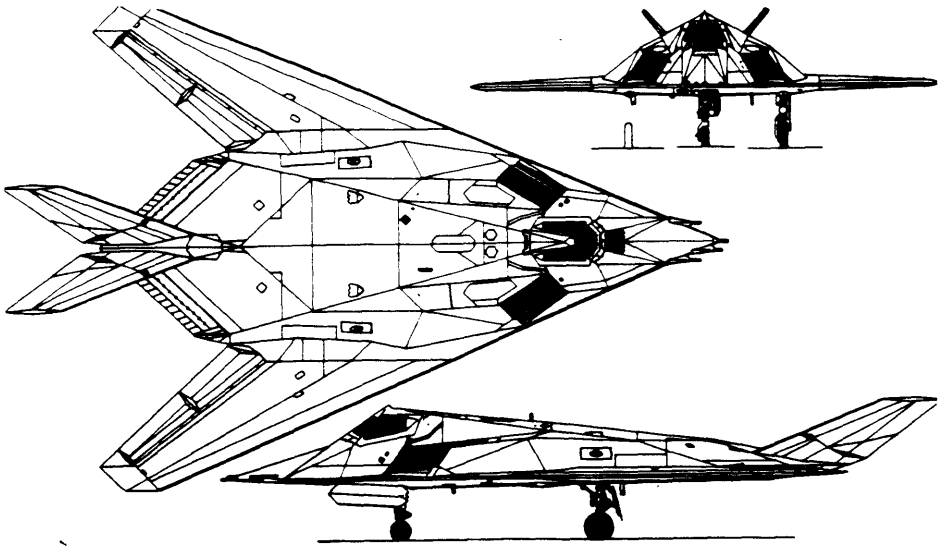

Figure 1.1: F117A Stealth Fighter

up of a number of flat surfaces, straight line wing and vertical tail leading edges, a continuous leading edge from nose tip to wing tip, a nearly flat fuselage undersurface, an extreme sweep angle of the tail surfaces, an unconventional hexagonal airfoil and flattened exhaust nozzles. Figure 1.1 is a picture of the F117A [8].

These features naturally lead to an interesting and complex vortical flow field. Since the flow solver used for this work is an inviscid Euler solver, it does not have the ability to model the separated flow associated with a boundary layer which would occur on an aircraft with more rounded surfaces.

1.1.2 Vortex Aerodynamics

A top view of the F117A reveals that the aircraft has the same basic geometrical features as those of a delta wing with a sweep angle of 68 deg. Because of its highly swept wings and sharp leading edges, flow separation from the leading edge is expected at moderate and high angles of attack. As a result, a pair of vortices is formed above the upper surfaces of each of the wings. The size and the strength of the vortices increase with angle of incidence and at high angles they become a dominant feature of the flow.

Vortical flows have a significant effect on the aerodynamic performance of the aircraft. If the vortices are both symmetric and stable, a large increase in normal force is observed which can be used as an aerodynamic advantage. However, phenomena like vortex breakdown and the occurrence of asymmetric vortices may produce large and sudden changes in the aerodynamic performance of the aircraft. Since the F117A is a modern fighter aircraft, its high angle of attack performance is very crucial during combat and maneuvering [13]. An in depth study of the vortical flow behavior is therefore crucial to its success.

1.1.3 Vortex Breakdown

At large angles of attack, it is expected that breakdown of the vortices occurs near the trailing edge. One obvious feature of vortex breakdown is a sudden enlargement of the vortex core [1]. This rapid increase in vortex diameter can be symmetrical (bubble-like) or asymmetrical (spiral-like). There are many theories as to the fundamental difference between the two forms of breakdown. One theory is that the spiral-like breakdown appears as a result of instabilities in the bubble form [4]. Figure 1.2 shows a visualization of the vortex breakdown over a delta wing as found by Lambourne and Bryer [9]. The lower vortex shows the axisymmetric bubble-type breakdown and the top vortex experiences the asymmetric spiral-type. Measurements of the axial velocity profiles done by Escudier showed that the breakdown occurs when the flow in the vortex reaches a stagnation point and forms a region of reversed flow [3]. Downstream of the breakdown, the flow is turbulent. Wind tunnel experiments by D. Hummel and P.S. Srinivasan [6] showed that vortex breakdown has an influence on the aerodynamic characteristics of the aircraft. Lift, drag and moment coefficients are significantly reduced due to the effect of bursting. Figure 1.3 shows the effect of breakdown on lift as found by Hummel and Srinivasan. They also determined that the position of vortex breakdown depends on the angle of attack. The location of vortex breakdown moves upstream as the angle of incidence is increased. Eventually, the bursting point crosses the trailing edge and lies above the wing.

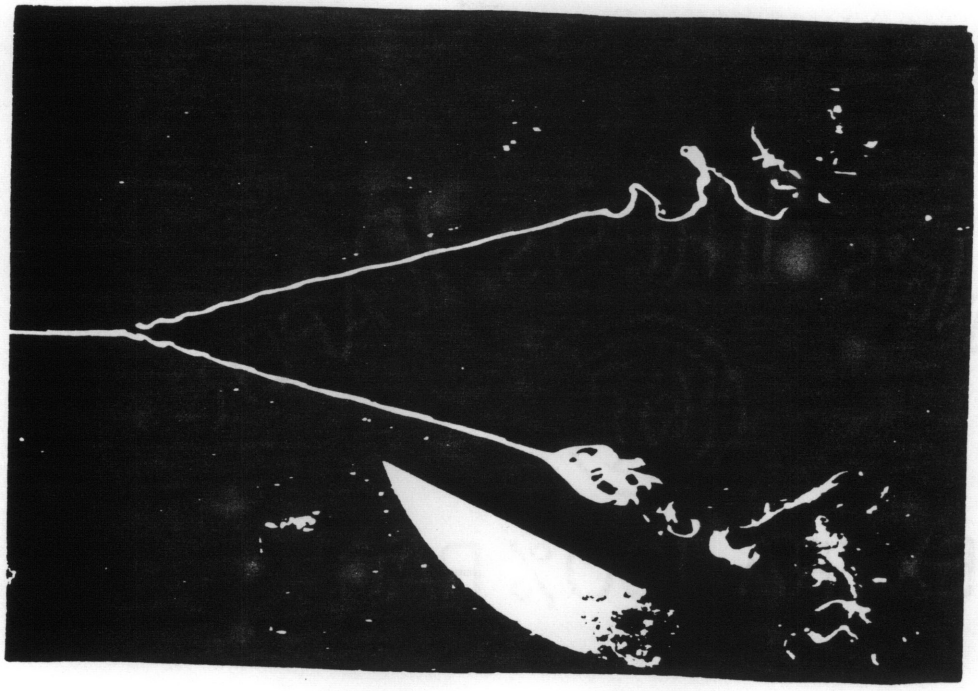

Figure 1.2: Flow visualization of a vortex breakdown

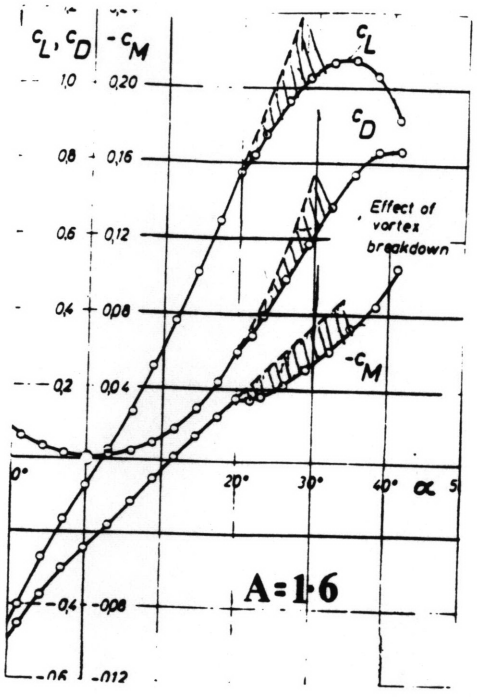

Figure 1.3: Effect of bursting on lift

1.2 Approach

This work presents the five main steps involved in a typical study of the flow characteristics of a complete aircraft. These five steps are :

- digital definition of model geometry
- three dimensional computational grid generation
- computational solution of equations of motion
- experimental data acquisition of flow characteristics
- comparison and discussion of results.

The following information on the F117A is known [8]:

- Wing span = 13.20 m (43 ft 4 in)
- Length overall = 20.08 m (65 ft 11 in)
- Height overall = 3.78 m (12 ft 5 in)
- Wing area = 105.9 sq m (1,140 sq ft).

The spatial discretization of the F117A is done by using a 1/32 scaled model of F117A. The grid generator uses unstructured meshes of tetrahedra in the three dimensional domain. A solution is obtained by running a three dimensional adaptive finite element Euler solver on the unstructured grid. Wind tunnel verification is done in a $5' \times 7'$ subsonic wind tunnel.

1.3 Thesis Summary

This investigation is performed to examine vortex breakdown and to observe the influence on the aerodynamic performance of the aircraft. The results of this study include computations of the flow at a range of angles of attack, comparisons with data from wind tunnel tests, and a detailed analysis of vortex breakdown. The main body of this

thesis consist of six chapters. In chapter two, the governing Euler equations and physical boundary conditions are described. The numerical solution procedure for the grid generator and the flow solver are discussed in chapter three. A detailed description of the advancing wave front method used for grid generation and the algorithms for the spatial and temporal discretization are described. The implementation of the boundary conditions and adaptative refinement method are also presented. Chapter four deals with the digital definition of the model geometry. The logical reasoning behind a simple surface definition and the geometry data acquisition system is described. Finally, the method used for mesh control is also presented in this chapter. In chapter five, the experimental procedure is discussed. Chapter six describes the results. A detailed analysis of each case is done. The experimental and computational lift and moment curves are found and the importance of grid adaptation on the solutions is verified. In chapter seven, conclusions are drawn and suggestions for future work are made.

Chapter 2
Governing Equations

This chapter formulates the governing Euler equations for the compressible flow of an inviscid ideal gas. This set of equations of motion represent conservation of mass, momentum and energy in a flow. In addition, the nondimensionalization of the equations and the physical boundary conditions will be discussed.

2.1 Theoretical Model

For sufficiently large Reynolds numbers, the viscous effects of a flow field are confined to a thin boundary layer near the surface of a solid boundary. Under these conditions, it is possible to solve the inviscid portion of the flowfield independently of the boundary layer, if the interaction between the boundary layer and the inviscid portion of the flowfield is negligible. This is the case for the computations over the F117A at high angle of attack. Eventhough they do not represent the physical viscosity of the flow, the Euler equations are still suitable for modeling separated flow. The sharp leading edges of the F117A are sufficient to enforce the Kutta condition with the artificial viscosity introduced into the solution method provides the necessary mechanism for leading edge separation. Because it is not our interest to model the boundary layer, an inviscid flow solution scheme is chosen over a Navier-Stokes scheme. CPU time is saved because it is unnecessary to obtain the high resolution in the viscous region of the flow as would be the case with the Navier Stokes equations.

2.2 Conservation Equations

The general expression for the conservation of a property B can be written as follows :

$$\frac{d}{dt}(\vec{B}_{sys}) = \frac{d}{dt}(\iiint \vec{\beta}\rho dV)_{CV} + (\iint \vec{\beta}\rho(\vec{u}\cdot\vec{n})dA)_{CS} \tag{2.1}$$

where $\beta = \frac{dB}{dm}$. Since no mass is created inside the control volume and using the first law of thermodynamics, the conservation of mass, momentum and energy are as follows :

$$\frac{dm}{dt} = \frac{d}{dt}(\iiint \rho dV) + (\iint \rho(\vec{u}\cdot\vec{n})dA) = 0 \tag{2.2}$$

$$\frac{d(m\vec{u})}{dt} = \frac{d}{dt}(\iiint \vec{u}\rho dV) + (\iint \vec{u}\rho(\vec{U}\cdot\vec{n})dA) = \sum \vec{F} \tag{2.3}$$

where $\vec{F}$ are the forces acting on the body

$$\frac{dE}{dt} = \frac{dQ}{dt} - \frac{dW}{dt} = \frac{d}{dt}(\iiint e\rho dV) + (\iint e\rho(\vec{u}\cdot\vec{n})dA) = 0 \tag{2.4}$$

where E, e, Q, W are energy, energy per unit mass, heat into the system and work by the system respectively. By using the divergence theorem, these equations can be written in the differential form and they become :

$$\frac{\partial\rho}{\partial t} + \nabla\cdot(\rho\vec{u}) = 0 \tag{2.5}$$

$$\frac{\partial(\rho\vec{u})}{\partial t} + \vec{u} \cdot \nabla(\rho\vec{u}) + \nabla p = 0 \tag{2.6}$$

$$\frac{\partial(\rho E)}{\partial t} + \vec{u} \cdot \nabla(\rho E + p) = 0. \tag{2.7}$$

2.3 Euler Equations

The compressible Euler equations in Cartesian coordinates without body forces or external heat addition can be written in vector form as :

$$\frac{\partial U}{\partial t} = -\Delta \cdot \vec{F} = -\frac{\partial F}{\partial x} - \frac{\partial G}{\partial y} - \frac{\partial H}{\partial z} \tag{2.8}$$

where the state vector U is :

$$U = \begin{bmatrix} \rho \\ \rho u \\ \rho v \\ \rho w \\ \rho E \end{bmatrix} \tag{2.9}$$

and the Cartesian components of the flux vector $\vec{F}$ are :

$$F = \begin{bmatrix} \rho u \\ \rho u^2 + p \\ \rho uv \\ \rho uw \\ \rho uh \end{bmatrix} \quad G = \begin{bmatrix} \rho v \\ \rho uv \\ \rho v^2 + p \\ \rho vw \\ \rho vh \end{bmatrix} \quad H = \begin{bmatrix} \rho w \\ \rho uw \\ \rho vw \\ \rho w^2 + p \\ \rho wh \end{bmatrix}. \tag{2.10}$$

The system is solved by using the equation of state for a perfect gas :

$$p = (\gamma - 1)\rho e \tag{2.11}$$

and by the definitions

$$e = E - \frac{1}{2}\left(u^2 + v^2 + w^2\right) \tag{2.12}$$

$$h = E + \frac{p}{\rho} \tag{2.13}$$

where ρ, u, v, w, E, p, h, e and γ are the density, Cartesian components of velocity, total energy per unit mass, pressure, total enthalpy per unit mass, internal energy per unit mass and ratio of specific heats, respectively.

2.4 Physical Boundary Conditions

Since we have a set of equations which are differential equations, a physically possible solution of the problem can only be found if appropriate boundary conditions are specified. For the solution of the Euler equations, three types of boundary conditions are specified. The implementation will be discussed in section 3.2.3.

2.4.1 Solid Wall Boundary Conditions

Since the F117A body is the only boundary to the fluid region, a solid wall boundary condition is needed on the F117A surface. Because the aircraft can be modeled as a solid wall, no fluid may pass through the boundaries. In this frame of reference, the

boundaries are at rest, and therefore, the boundary condition becomes :

$$\vec{u} \cdot \vec{n} = 0 \tag{2.14}$$

where $\vec{u}$ is the velocity of a fluid particle next to the wall and $\vec{n}$ is the unit normal to the wall surface. Since the calculation is only done on a half geometry, this condition is also imposed at the symmetry surface.

2.4.2 Kutta Condition

Because the Euler equations produce a set of more than one solution, extra conditions are needed to isolate a single solution to the differential equations. The Kutta condition is therefore enforced at the leading and the trailing edges of the body to fix the lift and to ensure a smooth flow over the trailing edge.

2.4.3 Farfield Boundary Condition

In the farfield the solution is forced to approach the conditions at free stream. Therefore, the following condition is enforced :

$$\vec{U} = \vec{U}_\infty. \tag{2.15}$$

2.5 Nondimensionalization

It is convenient to non-dimensionalize the governing equations. It clarifies which scales are important to the problem and it makes the solution independent of the choice of units. In addition, it often helps reduce the sensitivity of a numerical solution to round off errors. Table 2.1 gives the nondimensionalization of the flow quantities as used by Modiano [12]. It can be seen that the most important nondimensional parameters are the freestream Mach number, M_∞ and γ.

Quantity	Reference	Freestream Value
u,v,w	a_∞	$M_{X\infty}, M_{Y\infty}, M_{Z\infty}$
ρ	ρ_∞	1
p	ρa_∞^2	$1/\gamma$
E,h	a_∞^2	$M_\infty^2/2 + 1/\gamma(\gamma-1), M_\infty^2/2 + 1/(\gamma-1)$
x,y,z	L	- -
t	L/a_∞	- -

Table 2.1: Nondimensionalization of flow quantities

2.6 Auxiliary Quantities

The following is a list of relevant auxiliary quantities that can be defined in terms of primitive variables :

Quantity	Definition	Freestream
Local speed of sound	$a = \sqrt{\frac{\gamma p}{\rho}}$	1
Local flow speed	$q = \sqrt{u^2 + v^2 + w^2}$	M_∞
Local Mach number	$M = \frac{q}{a}$	M_∞
Total pressure	$p_o = p(1 + \frac{\gamma-1}{2}M^2)^{\frac{\gamma}{\gamma-1}}$	$\frac{1}{\gamma}(1 + \frac{\gamma-1}{2}M^2)^{\frac{\gamma}{\gamma-1}}$
Total pressure loss	$\Delta p_o = 1 - \frac{p_o}{p_{o\infty}}$	0
Entropy	$s = log\frac{\gamma p}{\rho^\gamma}$	0

Table 2.2: Nondimensionalization of flow quantities

Chapter 3
Numerical Solution Procedure

The grid generator used for this research work is part of the FELISA system which was developed by J. Peraire, J. Peiro and K. Morgan [14]. The inviscid flow solver used was written by D. Modiano at the Massachusetts Institute of Technology [12]. This chapter will first give a detailed description of the FELISA grid generation system and the advancing wave front method will be be discussed. Next, algorithms and methods for the spatial discretization, temporal discretization, implementation of the boundary conditions and adaptive refinement method will be discussed.

3.1 Grid Generation

3.1.1 The FELISA system

FELISA is made up of a set of five computer programs which allow the computation and simulation of three dimensional compressible steady inviscid flows using unstructured meshes of tetrahedral elements. FELISA consists of the following five main modules :

- a surface triangulator : SURFACE
- a three dimensional volume generator : VOLUME
- a flow solver preprocessor : PREPO
- an unstructured mesh flow solver : SOLVE
- a mesh adaptation procedure : ADAPT.

The modules used for this thesis work are SURFACE and VOLUME. The program SURFACE creates a triangular mesh on the boundaries of the three dimensional do-

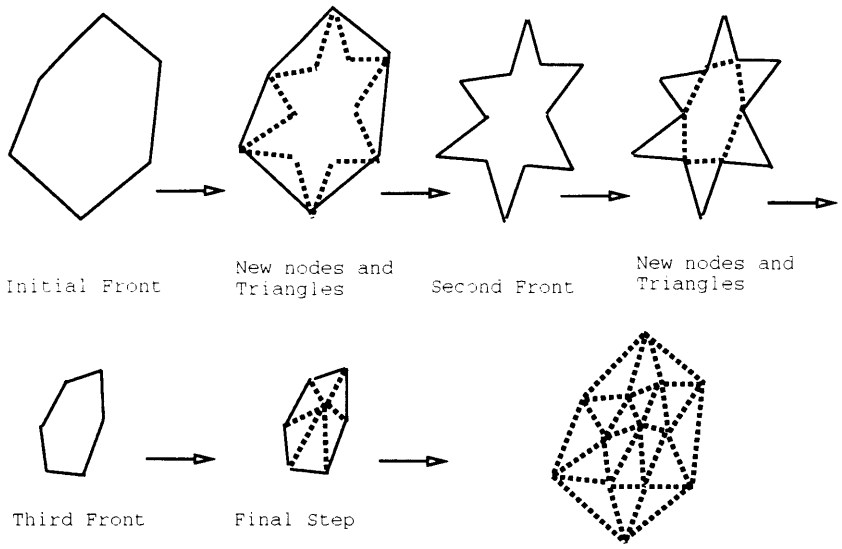

Figure 3.1: The Advancing Front Method

main. These boundaries are specified by the user with a surface definition file. In this file, the user defines support points and intersection segments of the surfaces which make up the body. Every surface is represented by four support points which determine the orientation and location of the plane. Intersection segments are the intersection lines between two adjacent surfaces. They are defined by two support points. The user also has the ability to specify the spatial distribution of the mesh parameters which are interpolated from a background grid made up of tetrahedral elements. The spatial parameters or sources define the spacing and the stretching of the tetrahedral elements in specific areas of the mesh. A more detailed description of the method for mesh control is given in section 4.5.1. The surface mesh is stored in a front file.

The program VOLUME uses the data file, the background file and and front file from SURFACE to create tetrahedra using the advancing wave front method in the three dimensional domain between the specified boundaries and creates a grid file.

3.1.2 FELISA : Algorithmic Details

The tetrahedral mesh generation method used in FELISA is the advancing wave front method [15]. A brief description of this method is given here. The triangular mesh generator SURFACE discretizes the boundaries which are specified in the first data file. This is the initial front. Next, by using the mesh spacing parameters as specified by the user in the background grid, a new node is created for each discretized segment and a triangle is formed. In some cases, an existing node is used if it satisfies the spacing parameters. Every new edge serves as a part of a new front. This continues until the complete 2-D space is discretized into triangles and a front file is created. The advancing front method is demonstrated in Figure 3.1. The tetrahedron volume generater VOLUME applies exactly the same technique in three dimensions. The front file created by SURFACE serves as the initial front. In the next step, a new node is created for every triangle and a tetrahedron is formed. Every new triangle serves as a new front. This is continued until the complete computational field is filled with tetrahedra. Figure 3.2 is an example of a surface grid created by FELISA with the advancing wave front method.

3.2 Flow solver

3.2.1 Overview

The solver for the Euler equations used for this research work was written Modiano [12]. It is a finite element Euler solver with an adaptive refinement by mesh point embedding. The method used to solve the governing equations is a Galerkin finite element discretization method. A four stage Runge-Kutta time-stepping scheme is applied for temporal discretization. Artificial dissipation is controlled by second and fourth difference terms. A pressure switch determines the amount of dissipation added. The second difference damping is turned on at sharp edges to enforce the Kutta Condition. In order to capture the important flow features, one level of adaptation by mesh point embedding is done.

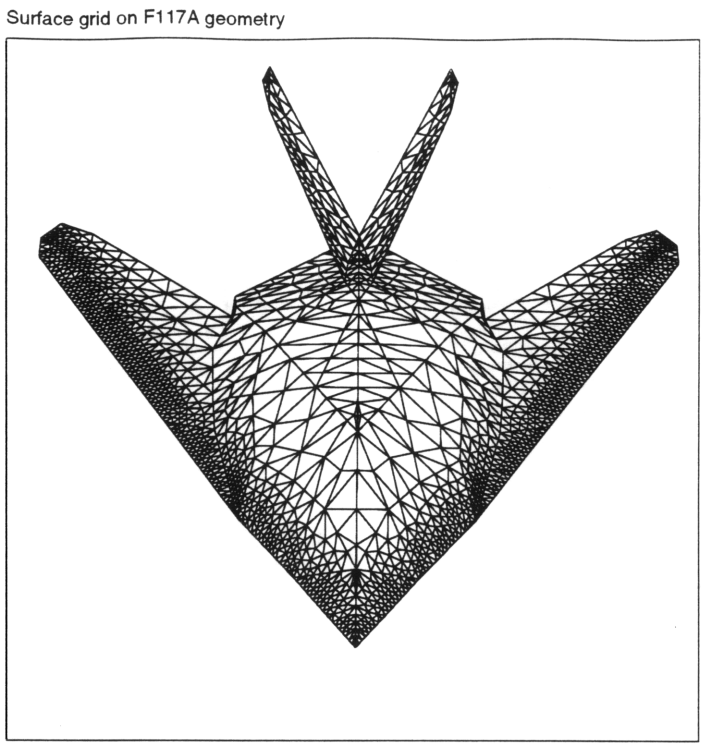

Figure 3.2: Surface grid on F117A by FELISA

Entropy is used for the adaptation parameter so that mesh points are added in regions where flow features have created entropy as for example in vortices.

3.2.2 Spatial Discretization

The conservation form of the Euler equations is used to perform the spatial discretization and it is written as

$$\frac{\partial U}{\partial t} = -\Delta \cdot \vec{F} = -\frac{\partial F}{\partial x} - \frac{\partial G}{\partial y} - \frac{\partial H}{\partial z} \tag{3.1}$$

where U is the state vector and F, G and H are the flux vectors. Spatial discretization is done by the Galerkin finite element method based on tetrahedral cells. In this method, the spatial variation of the state and flux variables is defined in terms of the nodal values of the quantities within each element, $U_i(t), F_i(t), G_i(t)$ and $H_i(t)$, and the local

interpolation functions $N_i(t)(x, y, z)$, so that

$$U(x, y, z, t) = \sum_i N_i(x, y, z) U_i(t) \tag{3.2}$$

$$F(x, y, z, t) = \sum_i N_i(x, y, z) F_i(t) \tag{3.3}$$

$$G(x, y, z, t) = \sum_i N_i(x, y, z) G_i(t) \tag{3.4}$$

$$H(x, y, z, t) = \sum_i N_i(x, y, z) H_i(t) \tag{3.5}$$

where i indicates a sum over the nodes of the element. The interpolation functions N_i are set to have a value of unity at the node i, and a value of zero at all other nodes. Modiano defines the local interpolation functions of each tetrahedron in terms of a set of four volume coordinates each one associated a node of the tetrahedron : ξ_1, ξ_2, ξ_3 and ξ_4. To define the volume coordinates, each tetrahedron of the mesh is arbitrarily divided into four smaller subtetrahedra. The four volume coordinates, are defined as the ratios of the volume of each subtetrahedron to the volume of the complete tetrahedron. As a result, since

$$\xi_1 + \xi_2 + \xi_3 + \xi_4 = 1 \tag{3.6}$$

ξ_4 can be replaced by $1 - \xi_1 - \xi_2 - \xi_3$ and the volume coordinates each can be given a value of unity at the node with which they are associated and a value of zero at the remaining nodes of the tetrahedron. Since this is a property desired by the interpolation functions, Modiano takes the interpolation functions to be exactly equal to the volume coordinates as described above.

For the spatial discretization of the Euler equations, the interpolated quantities of 3.2-3.5 are substituted in the Euler equations. The formulas for the derivatives in each element as a function of its nodal values are as follows :

$$\frac{\partial U}{\partial t} = \sum_i N_i \frac{dU_i}{dt} \tag{3.7}$$

$$\frac{\partial F}{\partial x} = \sum_i \frac{\partial N_i}{\partial x} F_i \tag{3.8}$$

$$\frac{\partial G}{\partial y} = \sum_i \frac{\partial N_i}{\partial y} G_i \tag{3.9}$$

$$\frac{\partial H}{\partial z} = \sum_i \frac{\partial N_i}{\partial z} H_i \tag{3.10}$$

When summing over all the elements in the domain, the following equation is obtained :

$$N_i \frac{dU_i}{dt} = -\frac{\partial N_i}{\partial x} F_i - \frac{\partial N_i}{\partial y} G_i - \frac{\partial N_i}{\partial z} H_i \tag{3.11}$$

where N_i is the sum of the interpolation functions of node i of each element that contains node i.

Since it is unlikely that assuming this form of a solution will satisfy the Euler equations at every point in the field, the weak form of the equations is found [20]. Instead of working with an equation that holds for each point, we need an equation that holds for a volume of the domain weighted by some function. This is done by projecting the equation onto the space of test functions $\tilde{N}_j$ and integrating them over the domain. For the Galerkin approach, these test functions are chosen identical to the interpolation functions at each node. The set of equations now looks as follows :

$$\frac{dU_i}{dt}\int N_i N_j dV = -F_i \int \frac{\partial N_i}{\partial x} N_j dV - G_i \int \frac{\partial N_i}{\partial y} N_j dV - H_i \int \frac{\partial N_i}{\partial z} N_j dV \qquad (3.12)$$

in which the repeated index i indicates summation over the set of nodes and the non-repeated index j space the set of the equations. Equation 3.12 can be rewritten as

$$M_{ij}\frac{dU_i}{dt} = -R_{X,ij}F_i - R_{Y,ij}G_i - R_{Z,ij}H_i \qquad (3.13)$$

where M_{ij} is the consistent mass matrix and $R_{X,ij}$, $R_{Y,ij}$ and $R_{Z,ij}$ are the residual matrices. These matrices are defined by integration over the entire domain. Since the test functions and the interpolation functions are defined piecewise with respect to each cell, Modiano breaks up the integrals by summing over the individual cells.

$$M_{ij}^C = \int_{V^C} N_i N_j dV \qquad (3.14)$$

$$R_{X,ij}^C = \int_{V^C} \frac{\partial N_i}{\partial x} N_j dV \qquad (3.15)$$

$$R_{Y,ij}^C = \int_{V^C} \frac{\partial N_i}{\partial y} N_j dV \qquad (3.16)$$

$$R_{Z,ij}^C = \int_{V^C} \frac{\partial N_i}{\partial z} N_j dV \qquad (3.17)$$

and the following equation is found

$$(\sum_{cells} M_{ij}^C)\frac{dU_i}{dt} = -(\sum_{cells} R_{X,ij}^C)F_i - (\sum_{cells} R_{Y,ij}^C)G_i - (\sum_{cells} R_{Z,ij}^C)H_i \tag{3.18}$$

where the range of summation is over the group of cells that contain node i. Modiano calculates the above matrices by performing a coordinate transformation into the local coordinate system (ξ_1, ξ_2, ξ_3) by applying the chain rule. The spatial derivatives of the volume coordinates are evaluated by representing the spatial coordinates x, y and z in the same way as the state quantities , i.e. via interpolation between the nodes. For example, for the x-coordinate in the local coordinate system :

$$x^C(\xi_1, \xi_2, \xi_3) = x_i N_i^C(\xi_1, \xi_2, \xi_3) = x_1\xi_1 + x_2\xi_2 + x_3\xi_3 + x_4(1 - \xi_1 - \xi_2 - \xi_3) \tag{3.19}$$

Now, the Jacobian matrix of transformation and its inverse are found

$$J = \frac{\partial(x, y, z)}{\partial(\xi_1, \xi_2, \xi_3)} \tag{3.20}$$

$$\Longrightarrow$$

$$J^{-1} = \frac{\partial(\xi_1, \xi_2, \xi_3)}{\partial(x, y, z)}. \tag{3.21}$$

As a result, $dxdydz$ translated into natural coordinates becomes

$$dxdydz \Longrightarrow \mid J \mid d\xi_1 d\xi_2 d\xi_3. \tag{3.22}$$

A more detailed description of the above procedure can be found in Appendix A.
The evaluation of the mass matrix then is fairly simple. When performing the coordinate transformation onto 3.14, the following is obtained

$$M_{ij}^C = \int_{V^C} N_i(x,y,z)N_j(x,y,z)dV$$
$$= \int_0^1 \int_0^{1-\xi_1} \int_0^{1-\xi_1-\xi_2} N_i(\xi_1,\xi_2,\xi_3)N_j(\xi_1,\xi_2,\xi_3) \mid J \mid d\xi_3 d\xi_2 d\xi_1. \quad (3.23)$$

Modiano determined that $\mid J \mid = 6V^C$ in which V^C is the volume of the cell (Appendix A). Because of geometrical symmetry, diagonal entries of the mass matrix are identical and off-diagonal entries are identical. The diagonal terms are

$$M_{ii}^C = M_{11}^C = 6V^C \int_0^1 \int_0^{1-\xi_1} \int_0^{1-\xi_1-\xi_2} N_1^2(\xi_1,\xi_2,\xi_3)d\xi_3 d\xi_2 d\xi_1$$
$$= 6V^C \int_0^1 \int_0^{1-\xi_1} \int_0^{1-\xi_1-\xi_2} \xi_1^2 d\xi_3 d\xi_2 d\xi_1$$
$$= \frac{1}{10}V^C \quad (3.24)$$

and the off-diagonal terms become

$$M_{ij}^C = M_{12}^C = 6V^C \int_0^1 \int_0^{1-\xi_1} \int_0^{1-\xi_1-\xi_2} N_1 N_2 d\xi_3 d\xi_2 d\xi_1$$
$$= 6V^C \int_0^1 \int_0^{1-\xi_1} \int_0^{1-\xi_1-\xi_2} \xi_1\xi_2 d\xi_3 d\xi_2 d\xi_1$$
$$= \frac{1}{20}V^C. \quad (3.25)$$

The residual matrices are also evaluated by performing the same coordinate transformation.

In order to obtain a solution using this method, one needs to find the inverse of the mass matrix. To simplify this process, Modiano forms a lumped mass matrix which

is essentially is a diagonalized mass matrix. This can then be inverted trivially. The lumped matrix is created by summing up all the terms of a row of the original mass matrix. This causes no loss of accuracy for this research work since only a steady-state time-asymptotic solution is desired.

It is now possible to combine all pieces and obtain the semidiscrete form of the Euler equations which is used for the solution procedure. The following equation is obtained. [12]

$$V_i \frac{dU_i}{dt} = -R_i \tag{3.26}$$

where V_i is the volume of the supercell of node i and R_i is the residual.

3.2.3 Numerical Boundary Conditions

The implementation of the boundary conditions is now described [12]. At a solid boundary, two boundary conditions are necessary. First, a restriction on the fluxes is imposed such that the non-pressure terms normal to the solid wall vanish. Modiano implements this condition by constructing a correction flux term to be added to all nodes which lie on a solid wall face or a symmetry face. Second, the velocity vector is forced to be tangent to the wall at every boundary face. Because of the inviscid nature of the flow, the boundary conditions at the symmetry surface are identical to those applied at a solid wall.

Modiano prescribes some special boundary conditions at edge boundaries and corner boundaries. An edge boundary is defined as " the intersection of two solid surfaces in the case that the solid body protrudes into the fluid, such as the trailing edge of a wing" [12]. At such a point, the flow has a tendency to become infinite. Numerically, artificial dissipation is sufficient to prevent this from happening and to enforce the Kutta condition. For sharp edges however, Modiano added a switch which turns on the second-difference smoothing at the edge nodes. A corner boundary on the other hand is described as

"the intersection of a symmetry surface with a solid surface , in the case that the fluid protrudes into the solid body" [12]. The boundary condition applied to such a corner is that the flow cannot have a normal component to either of the two intersection surfaces.

The farfield boundary conditions are based on the one dimensional characteristic theory. The Euler equations in three dimensions are transformed into a system based on coordinates normal and tangential to the boundary (n,b,t). The equations are then linearized and the assumption is made that the derivatives in the normal direction are much larger than those in the tangential direction. As a result, a one-dimensional partial differential equation is obtained. The system is diagonalized by assuming that the flow is locally isentropic. Landsberg [10] found that for vortex flows, this results in a good approximation and decouples the equations. The following characteristic equation is found

$$\frac{\partial C}{\partial t} = \Lambda \frac{\partial C}{\partial n}$$

where

$$\begin{bmatrix} C_1 \\ C_2 \\ C_3 \\ C_4 \\ C_5 \end{bmatrix} = \begin{bmatrix} J_+ \\ J_- \\ u_t \\ u_b \\ e^s \end{bmatrix} = \begin{bmatrix} u_n + \frac{2a}{\gamma - 1} \\ u_n - \frac{2a}{\gamma - 1} \\ (\vec{u} - u_n \vec{n}).\vec{t} \\ (\vec{u} - u_n \vec{n}).\vec{b} \\ \frac{p}{\rho^\gamma} \end{bmatrix} \tag{3.27}$$

where J_+ and J_- are the Riemann invariants and s is the entropy.

The characteristic variable J_+ is convected normal to the boundary at a velocity $u_n + a$ and J_- is convected normal to the boundary at velocity $u_n - a$. In order to avoid the necessity of computing the tangential coordinate directions, the tangential velocity is kept as a vector, $\vec{u}_t$. The characteristic wave speed associated with $\vec{u}_t$ and e^s is u_n. The sign of the wave speed determines whether the characteristics are convected outward from the domain or inward from outside of the domain. It is then clear whether they are calculated from the internal quantities or the external boundary conditions

prescribed. If $0 < u_n < a$ the boundary represents an inflow which is subsonic, therefore, J_+, e^s and $\vec{u_t}$ propagate into the domain while J_- propagates out of the domain. A subsonic outflow exists when $-a < u_n < 0$ in which only J_+ is convected from the exterior into the domain. For $u_n > a$ which represents a supersonic outflow, all characteristics enter the domain as specified by the boundary conditions and for an inflow $(u_n < -a)$ all characteristics propagate out of the domain and no conditions need to be specified.

3.2.4 Artificial Dissipation

Artificial dissipation or smoothing is necessary to stabilize the numerical scheme and to damp out the disturbances in the background [12]. The dissipation at a node i is a combination of second- and fourth-difference terms and can be written as follows

$$D_i = D(U_i) = \mathcal{D}(\kappa_2 \mathcal{D} U_i - \kappa_4 \mathcal{D}(\mathcal{D}^2 U_i)) \tag{3.28}$$

where $\mathcal{D}$ and $\mathcal{D}^2$ are first and second difference operators respectively and the second- and fourth difference terms are defined by

$$\kappa_2 = \frac{V}{\Delta t_{max}} s\varepsilon_2 \tag{3.29}$$

$$\kappa_4 = \frac{V}{\Delta t_{max}} (1 - s)\varepsilon_2. \tag{3.30}$$

The amount of second and fourth difference dissipation is determined by a pressure switch which is calculated at each node

$$s_i = \frac{|\ \mathcal{D}^2 p_i\ |}{p_i}. \tag{3.31}$$

The Kutta condition is imposed by using only second difference smoothing. This is done by setting the switch s_i to unity at the sharp edge where the Kutta condition is required. The quantities ε_2 and ε_4 are empirical coefficients which control the second- and fourth difference dissipation. They are needed to achieve a rapid convergence without corrupting the solution.

3.2.5 Temporal Discretization

A four-stage modified Runge-Kutta time-stepping scheme is used :

$$\begin{aligned}
U_i^{(0)} &= U_i^n \\
U_i^{(1)} &= U_i^{(0)} + \alpha_1 \frac{\Delta t_i}{V_i}(-\lambda R_i^{(0)} + D_i^{(0)}) \\
U_i^{(2)} &= U_i^{(0)} + \alpha_2 \frac{\Delta t_i}{V_i}(-\lambda R_i^{(1)} + D_i^{(1)}) \\
U_i^{(3)} &= U_i^{(0)} + \alpha_3 \frac{\Delta t_i}{V_i}(-\lambda R_i^{(2)} + D_i^{(2)}) \\
U_i^{(4)} &= U_i^{(0)} + \alpha_4 \frac{\Delta t_i}{V_i}(-\lambda R_i^{(3)} + D_i^{(3)}) \\
U_i^{n+1} &= U_i^{(4)}
\end{aligned} \tag{3.32}$$

where $\alpha_1 = \frac{1}{4}$, $\alpha_2 = \frac{1}{3}$, $\alpha_3 = \frac{1}{2}$, $\alpha_4 = 1$, Δt is the time step, $D_i^{(0)}$ is the artificial dissipation and $R_i^{(0)}$ is the residual at stage zero. Note that Modiano [12] separates the CFL number λ from the time step Δt . This was done to prevent the dissipation from being scaled by the CFL number. In this manner, similar stability characteristics will be observed with changing CFL number. In this scheme, the residuals are recalculated at every stage. The fourth difference dissipation can be frozen at the first stage but the

second difference dissipation must be evaluated at the second stage also. The time step is evaluated at each node and each Runge-Kutta stage. Local time stepping is used to accelerate the convergence, so that Δt_i varies for each node.

3.2.6 Adaptive Refinement Method

Adaptation is used to increase the resolution of certain flow features and at the same time to save computational costs by refining the grid only in specific areas of the mesh. First, a solution which roughly captures the important features of the flow is found on a coarse grid. After the solution has evolved to some point on the coarse grid, an adaptation parameter is calculated at the mesh nodes.

In order for adaptation to be relevant, the chosen adaptation parameter needs to reflect the nature of the expected flow features. By doing this, one can easily locate the regions in the computational domain where the grid requires refinement. In the case of vortex flows, as for the F117A geometry, entropy may be used as the adaptation parameter. The fact that entropy is uniform in a steady irrotational flow but leading edge vortices include significant entropy production allows the user to locate the nodes associated with extreme values of entropy inside the vortex and indicate them for adaptation.

Adaptation is done by mesh-point embedding. With this node-based method, the nodes from the coarse grid are kept in their original locations and new nodes are added at the centers of the edges of which both nodes were indicated for adaptation. The refinement of the triangles can by done in several ways. The choice of method as used by Modiano depends on the number of nodes of the triangle which were marked by the adaptation indicator [12]. The refinement of the tetrahedral cells depends on the structure of the mesh in a similar way, except more complicated.

Chapter 4

F117A Digital Definition

Computing the Euler equations over a complex configuration requires a detailed description of the aircraft geometry. Since no CAD data for the F117A were available, a simple surface definition was developed and the aircraft geometry data were taken manually with the help of a micrometer and a milling machine.

4.1 Simple Surface Definition

In order to write the surface definition file for the modules SURFACE and VOLUME, the spatial coordinates for the aircraft need to be specified. A 1/32 scale model of the F117A was used to obtain them. The engine inlet and outlet have been replaced by solid surfaces. To simplify the complex geometry, it is assumed that the aircraft consist of 78 support surfaces with 76 nodes connecting them. Each of the support surfaces is defined by at least three node points. Figure 4.1 shows the simple geometry description.

4.2 Data Acquisition

The spatial coordinates for each of the corner points were measured with the help of a milling machine and a micrometer. These allow the user to determine the relative 3-D coordinates of points on a body. The set up is shown schematically in Figure 4.2. Since the F117 is a perfectly symmetric airplane, only half of the necessary nodal points are measured. The location of a total of 38 points is determined and then projected about the symmetry plane.

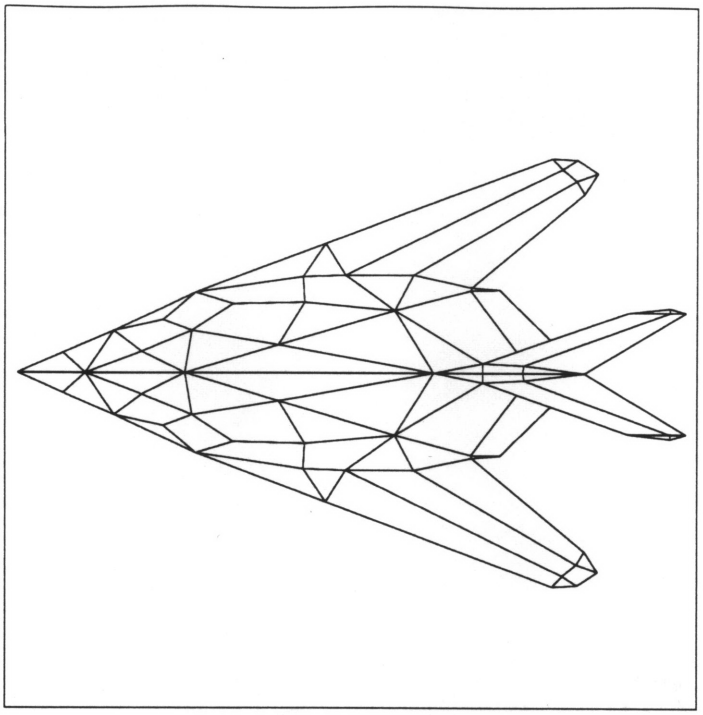

Figure 4.1: Simple Geometry Description

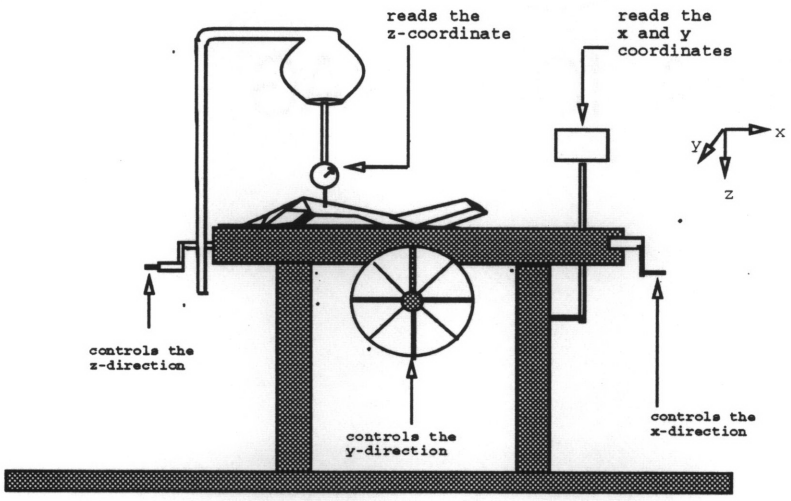

Figure 4.2: Set up for acquisition of spatial coordinates

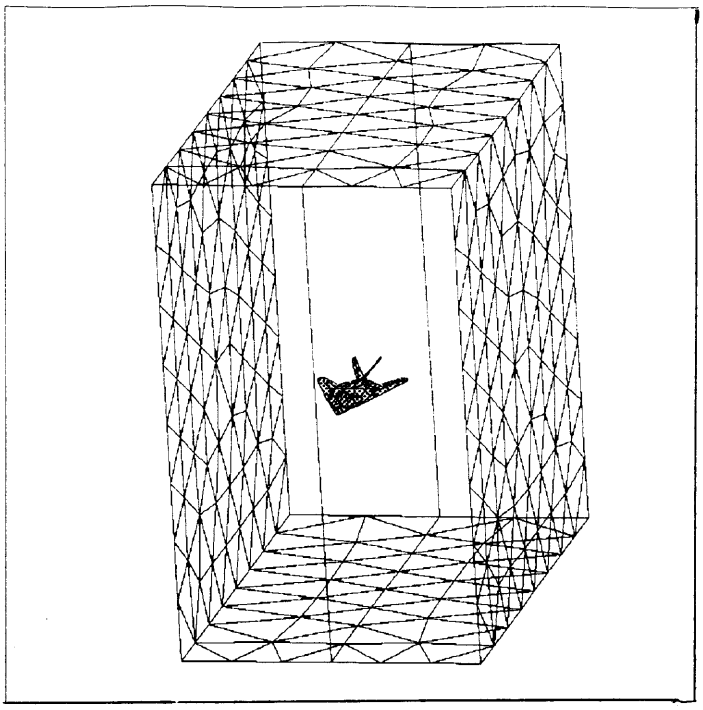

Figure 4.3: Farfield Boundary

4.3 Farfield Boundary

The farfield boundary which represents the outer edge of the computational domain consists of a rectangular prism. It is located three span lengths away from the symmetry plane, one length of the aircraft distance in front of the aircraft and three lengths behind the F117A. Figure 4.3 shows the farfield boundary used for all calculations.

4.4 Error Correction by FELISA

Because the data for the geometry of the F117A are measured manually, there are small errors in the spatial coordinates of each of the measured points. When defining the intersection segments and the support points for the surfaces in the surface definition file, the four nodes which are representing a surface are not correctly defining a flat plane due to a measurement error. The module SURFACE corrects this error by calculating an average surface and projecting the four nodes on the new surface.

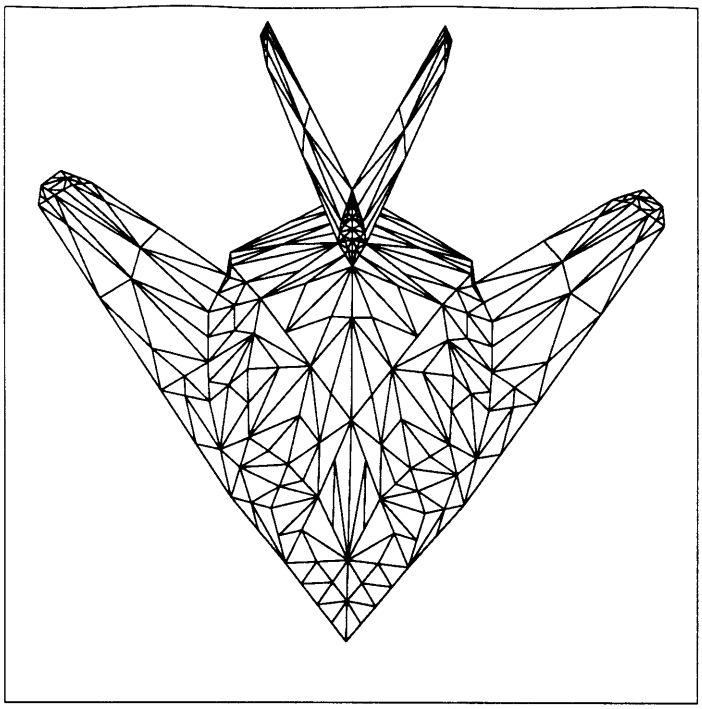

Figure 4.4: Simple Surface Grid

Figure 4.4 shows a simple grid as it was created by SURFACE. It is obvious that this particular triangulation was not very successful : the grid is very coarse and the triangles on the wings and vertical tails show very sharp angles. This can be corrected by setting the mesh spacings for certain areas in the computational grid. As described in the next section, it is done by specifying a number of sources in the background grid.

4.5 Background Grid

The background grid used to produce Figure 4.4 contains no specific mesh parameters. The grid is a very simple one. It consist of four grid nodes which make up one tetrahedral element. As shown in Figure 4.5, the nodes of the element are specified far away from the computational domain, such that the background tetrahedral element completely encloses the F117A and the farfield domain.

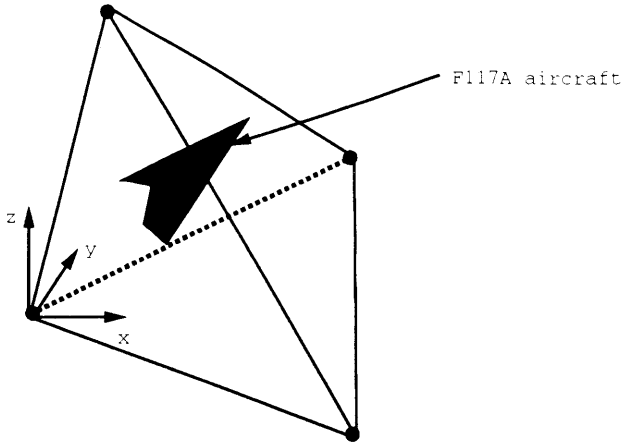

Figure 4.5: Farfield Overview

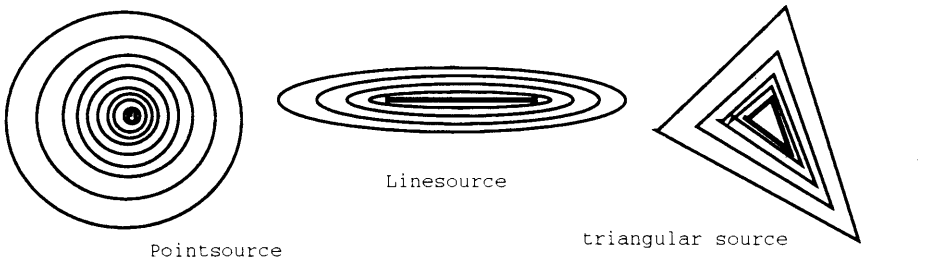

Figure 4.6: Point, Line and Triangular Sources

4.5.1 Mesh Spacing Parameters

The background grid also allows the user to specify three types of mesh spacing specifications ; point sources, line sources and triangle sources as represented in Figure 4.6. For a point source, one specifies the 3-D location of the source and three parameters : s1, d1 and d2. S1 sets the spacing of the grid right at the source. The variation of the spacing with distance from the source is given by parameters d1 and d2. As shown in Figure 4.7, d1 represents the distance from the source within which the spacing is constant and equal to s1. D2 is the distance from the source for which the spacing is twice the spacing at the source. Between d1 and d2, the spacing varies exponentially between s1 and $2 \times s1$. Line and triangular sources are shown in Figure 4.6. A line source is defined by two point sources and a triangular source is defined by three point sources. The spacings are specified in a similar manner. Linear interpolation of s1, d1 and d2 is used between each of the points defining the lines and triangles and the distances are the distances perpendicular to them. This results in an isotropic distribution of the

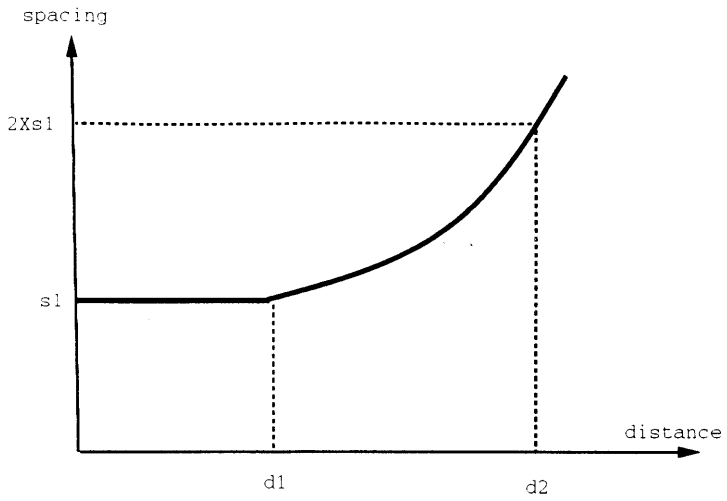

Figure 4.7: Parameters used to control spacing

mesh spacing.

4.5.2 Location of Sources

The locations of the point, line and triangle sources in the background grid are shown in Figure 4.8. In order to create a grid which is finer on the surface of the aircraft and coarser in the far field of the computational domain, a point source is defined in the middle of the F117A and a triangular source is wrapped around the edge of the aircraft geometry. As can be seen in Figure 4.1, the support surfaces which represent the vertical tail and the wing tip are very small in size relative to the other surfaces. In order to obtain a grid fine enough for these support surfaces, four line sources are placed on the fin and one on the wing tip. The grid on the sharp leading and trailing edges is refined by defining a total of five line sources. The final grid obtained from this background grid is shown in Figure 4.9.

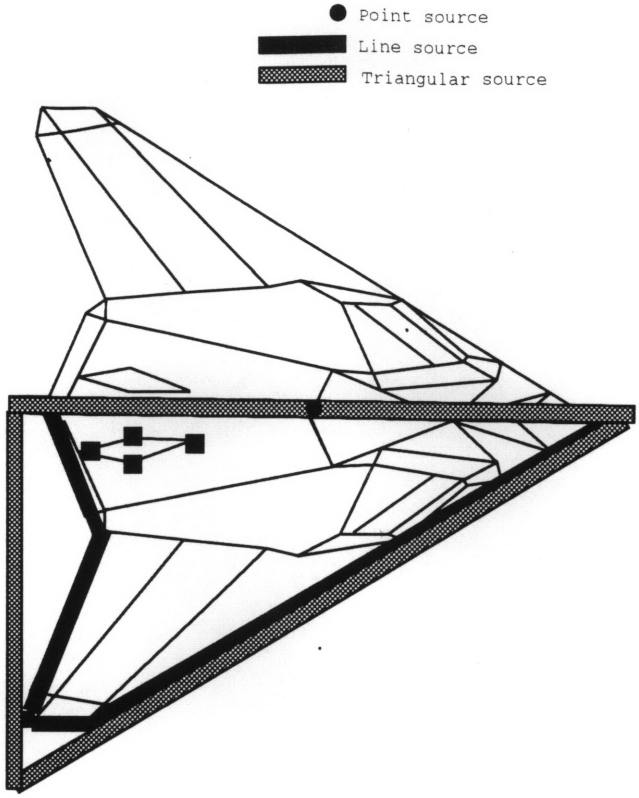

Figure 4.8: Location of the sources for F117A

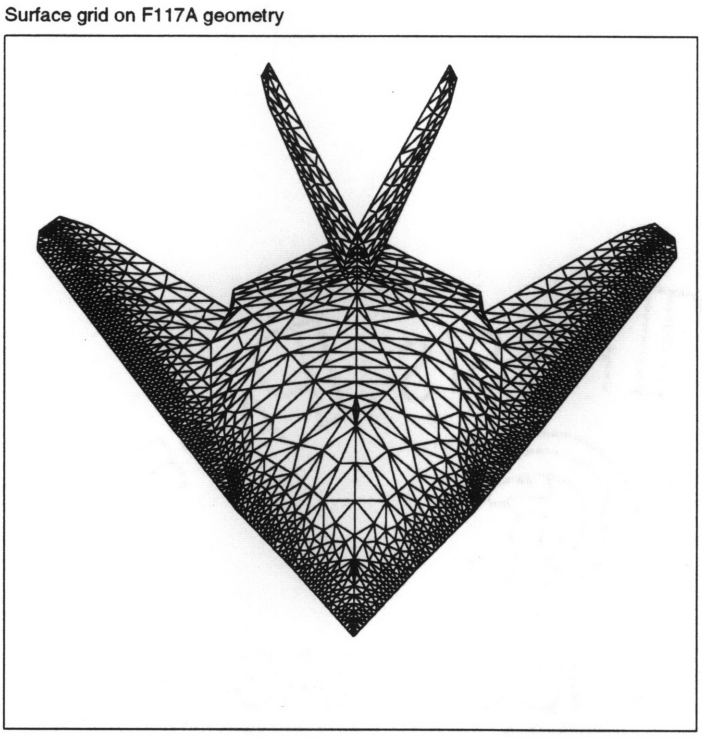

Figure 4.9: Farfield Boundary

Chapter 5
Wind Tunnel Testing

In order to verify the computational results for this research work, wind tunnel tests are done to obtain experimental lift and moment curves for the F117A. Smoke and laser technique visualization are also performed for high angles of attack in order to determine the location of vortex breakdown. The location of breakdown is compared to the location obtained through computations. Force data are obtained using a wire balance force measurement system and a 1/32 scale model of the F117A in the subsonic $5' \times 7'$ wind tunnel at MIT. In this chapter, a general description of the experimental set up is given. The construction of the model, the installation in the tunnel and the data acquisition system will be described in detail.

5.1 Experimental Procedure

5.1.1 Construction of F117A Model

The model used for the wind tunnel tests is a 1/32 scaled model of the F117A stealth fighter identical to that described in section 4.1. It is a fragile plastic toy model, not designed to meet the demands of wind tunnel testing. It is therefore necessary to increase the weight and the strength of the model. This is done by bracing the plane internally with wood and then filling it up with epoxy and foam. Increasing the mass makes the model more stable and therefore allows measuring the data in more reliable fashion. At the same time, the addition of hard points ensures that the model can withstand the forces exerted during high wind speeds and high angles of attack.

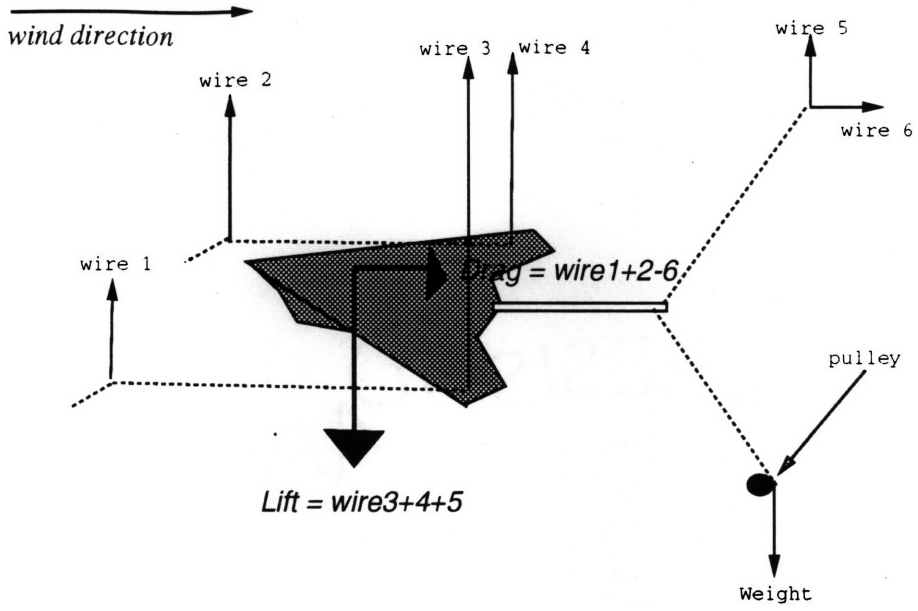

Figure 5.1: Experimental Set Up in Acoustic Wind Tunnel

5.1.2 Experimental Set Up

The strengthened 1/32 scaled model is placed upside down in a open jet wind tunnel of dimensions $5' \times 7'$ feet. The tunnel has the capacity to produce winds up to 80 miles per hour (Mach 0.1). The forces on the model are measured with a wire balance and a computerized force measurement system. Figure 5.1 shows the experimental set up.

As shown, the wire balance system consists of a set of thirteen wires. Each of them has a very specific location and function for the measurement of the aerodynamic forces on the aircraft. The locations are determined based on the ability of the chosen set up to keep the model steady in the tunnel during a run. The function of each wire becomes clear when studying Picture 5.1. The lift on the model is represented by the total strain in wires 3, 4 and 5. When subtracting the strain in wire 6 from the total strain in wires 1 and 2 one can determine the total drag on the aircraft. By suspending the model upside down, the weight of the plane and the lift force point in the same direction. This makes the model more stable and consequently makes the read out of the data more

reliable.

Strain gauges or load cells are the primary tools used in determining the strain in each the wires. Each cell is connected to a controller which includes a power supply, sensitive voltmeters and potentiometers to control the sensitivity and the balance of the cells. Each strain gauge is calibrated individually and a conversion factor of pound force per volt is calculated and assigned to the location. The calibration of each wire is done as follows : first, the sensitivity dials for each wire were set according to preliminary estimations for lift and drag forces. Then, a number of weights are suspended and the voltage corresponding to each weight is recorded. The slope of the volt versus force curve corresponded to the conversion factor. This is automatically done by a computerized data acquisition system equipped with the necessary software to take the readings from the strain gauges during each run. The specialized software package, when supplied with the conversion factor for each wire, reads about 1000 sample measurements of the tunnel speed and the voltage of each cell. It then calculates the average forces for each wire and subsequently it determines the total lift and drag on the F117A.

5.1.3 Visualization

In order to observe the vortex and the angle of attack at which vortex breakdown first occurs, flow visualization is done. A smoke nozzle is placed in front of the aircraft model in such a way that it is easily adjustable. To provide a better view of the breakdown and its location, a laser beam pointing at the smoke is diffracted into a planar sheet normal to the flow direction. This technique is very suited for the visualization of the vortex in the breakdown region. Both the smoke nozzle and the laser beam are placed at several locations in order to achieve an optimum visualization.

5.2 Test Matrix

Table 5.1 is a summary of wind tunnel tests done. The tunnel is at three tunnel velocities in order to determine the Reynolds number effects on the lift and the pitching moment slopes at high angles of attack. Pope reports that in general, pressure distributions at low angles of attack and the slope of the lift curve seem almost unaffected down to Reynolds number down to 200,000 [17]. Since the tunnel is operated at a Reynolds number exceeding 200,000, see Table 5.1, Reynolds number independence is expected.

Mach Number	Reynolds Number	Wind Speed	Angle of attack (deg)
0.04	6×10^5	13 m/sec	7-10-15-20-25
0.06	9.26×10^5	20 m/sec	7-10-15-20-25
0.08	1.23×10^6	27 m/sec	7-10-15-20-25

Table 5.1: Test matrix for wind tunnel verification

Chapter 6

Results

This chapter presents the final results of the computational and experimental work for this research. It deals more in depth with the computations and the adaptation criteria used. An overview of all cases and the grids associated with them is given. Additionally, a detailed analysis of the computed solutions is discussed. A comparison of lift and moment curves obtained though CFD with the experimental curves serves as a verification for the accuracy of the computations. Finally, the effects of adaptation on the solutions will be discussed.

6.1 Introduction

Since our main interest is to compare solutions at a variation of angles of attack and to observe vortex breakdown, all calculations and wind tunnel tests are for zero yaw. Figure 6.1 [16] shows the conditions under which vortex breakdown occurs on a delta wing for incompressible conditions. Λ is the sweep angle and α is the angle of attack. Since the planform of the F117A is basically a delta wing of Λ 68 degrees, Figure 6.1 shows that there will be no vortex asymmetry. Therefore, to save CPU time, the solutions are found on half of the geometry and projected around the symmetry plane.

All calculations are done on a CRAY X-MP EA/464. Calculations in this thesis consumed up to 12 hours of CPU processing time. The RMS of error is calculated in the following manner :

$$RMS = \sqrt{\frac{1}{5N} \sum \left(\delta U_1^2 + \delta U_2^2 + \delta U_3^2 + \delta U_4^2 + \delta U_5^2\right)}$$

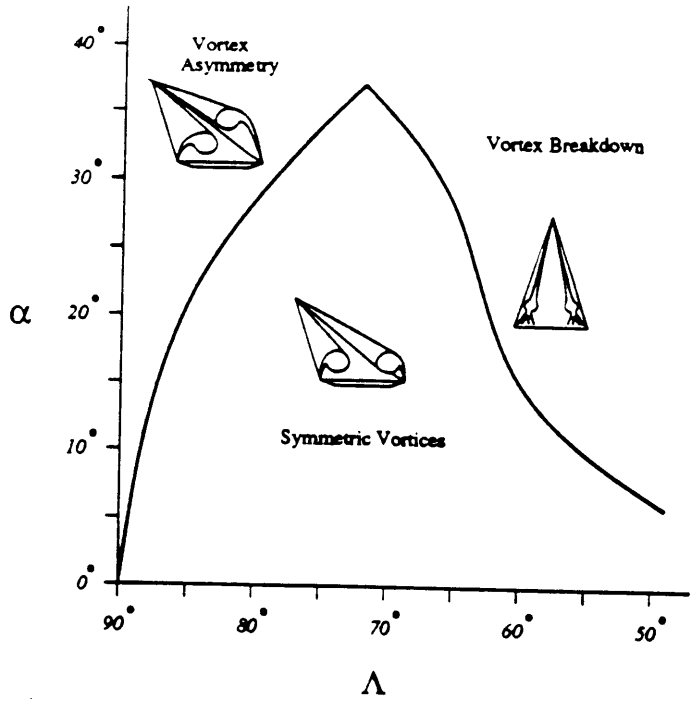

Figure 6.1: Vortical behavior over delta wing in incompressible flow

where N is the number of nodes in the grid and δU_i^2 is the change of component i of the state vector at each node between to consecutive iterations. Convergence of the unadapted solution is reached when the RMS errors have reached 10^{-5} or smaller. Since solutions at high angle of attack on an adapted grid result in vortex breakdown, converged solutions were not obtained. This does not mean that the calculation diverges, but it is simply a result of localized vortex instabilities due to vortex breakdown. Since the breakdown location is not fixed, these calculations are assumed to be unsteady, and no steady state can be obtained. The unsteadiness is therefore observed in the RMS : it quickly drops to a minimum which is much larger than machine precision, and then it settles into a cycle of oscillations where the RMS oscillates between a minimum and a maximum value.

Visualization is done with a three-dimensional visualization package VISUAL3, an interactive package developed by Haimes [5]. The results presented in the next sections are visualized for the reader by orienting cutting planes at several locations along the symmetry axis of the aircraft as shown in Figure 6.2. The resultant two-dimensional data mapped onto the planar cut will be shown. Also, streamlines which are curved 3D lines parallel to the local velocity field are used to determine whether or not vortex

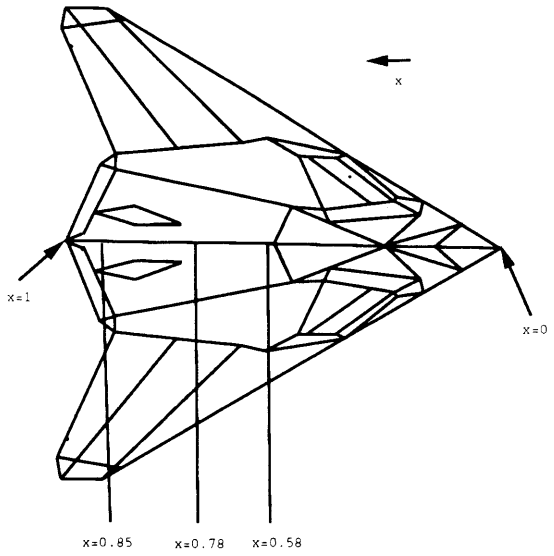

Figure 6.2: Location of cutting planes

breakdown has occurred.

In order to observe the vortical behavior of the flow, contour plots of total pressure loss are mapped onto planar cuts oriented at various stations in the computational domain. Total pressure is a reasonably good measure of the vortex structure, strength and location. It is usually expressed as total pressure loss, defined as :

$$\Delta p_0 = 1 - \frac{p_0}{p_{0\infty}}. \tag{6.1}$$

It is clear that total pressure loss far away from the vortex is 0 and the maximum possible total pressure loss is 1.

Solutions are found for seven angles of attack in the range of zero to 30 degrees. Calculations are performed on both an unadapted and adapted grid for each case.

6.2 Grid Adaptation

Table 6.1 gives a summary of the computational grid used for each of the cases. Before producing a finer and more regular grid, a solution must first be found on the coarse

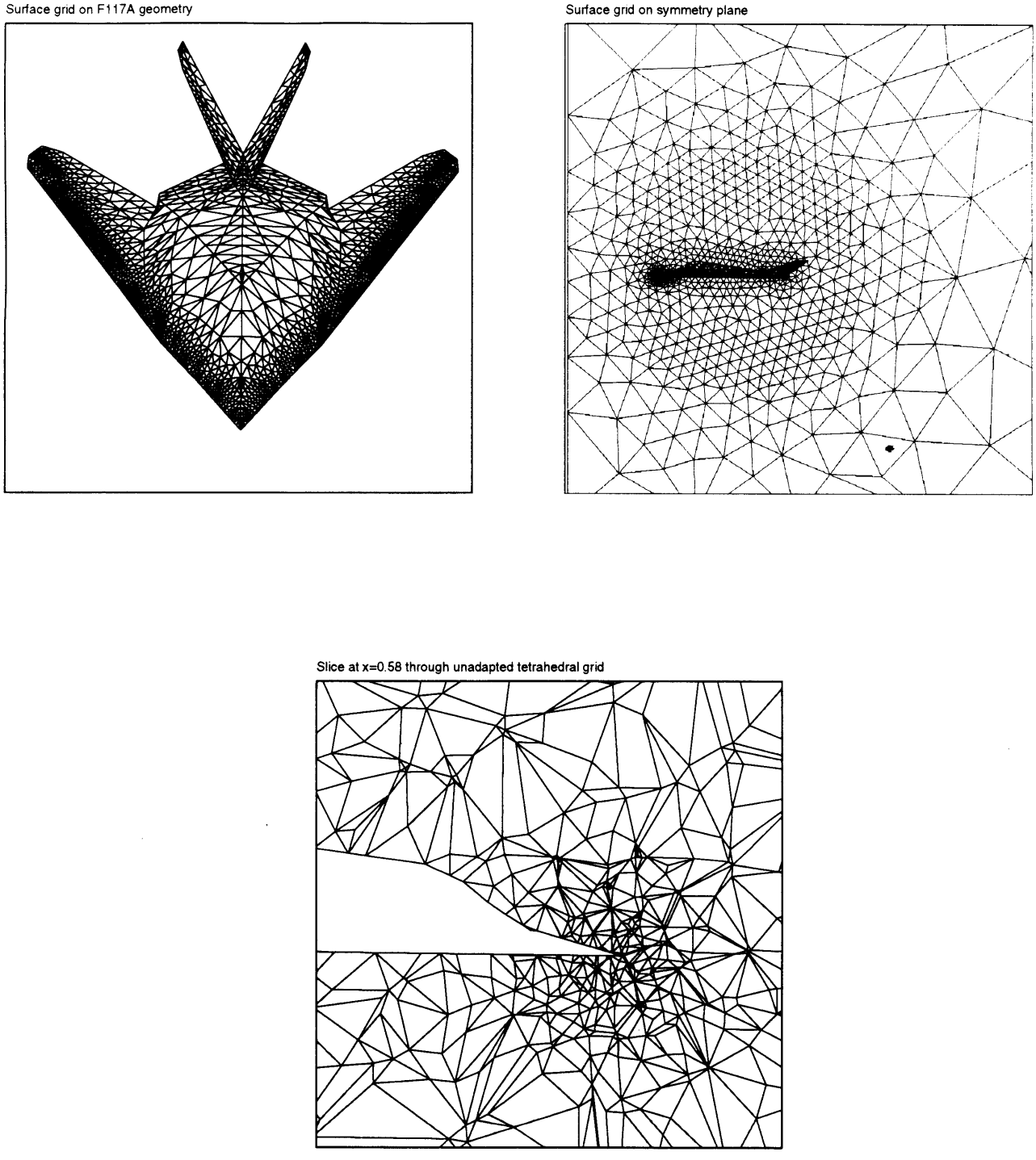

Figure 6.3: Surface grid, symmetry plane and slice for coarse grid created by FELISA

Case	Nodes	Cells	Cell/Node
7 deg	45,271	222,234	4.91
10 deg	44,764	220,322	4.92
15 deg	49,531	244,973	4,94
20 deg	48,518	240,122	4.95
25 deg	48,724	241,400	4.95
30 deg	47,036	233,135	4.95

Table 6.1: Matrix of grids for computations

grid which is shown in Figure 6.3. This original grid, created by FELISA contains 9,396 nodes and 48,316 cells. On the left is the surface mesh of the F117A. The grid density on the symmetry plane is shown in the next picture. Additionally, the mesh on a planar cut sliced at 58% of the length of the aircraft is represented in the final picture. Using the results from this unadapted grid, one level of adaptive refinement is performed for all angles of attack. As described in section 3.2.6 fluid entropy is used as the adaptation parameter, with the criterion that approximately 30% of the nodes be chosen for adaptation. Figure 6.4 shows the effect of adaptation on the grid. Clearly, when comparing it to the coarse grid, the adaptation procedure has allowed for a refinement of the mesh along the leading edge of the aircraft and above the wing where the vortex has formed.

The calculations were approached as follows. First, calculations at 7, 10, 15 and 20 degrees were performed on the unadapted grid. Adaptation was next performed on the 20 degree case and vortex breakdown was observed. Because the breakdown region appeared just at the trailing edge of the wing, it was clear that 20 degrees was the lower range of angles where breakdown occurs. With the goal of observing breakdown at a more upstream location, two more adapted calculations at higher angles of attack, i.e. 25 and 30 degrees were performed. Finally, to obtain a better resolution, adaptation was also done for the 7,10 and 15 degree case. A summary of the adapted grid for each case is presented in Table 6.1. The effect of the adaptation on the solutions will be reported and analyzed in section 6.3.3.

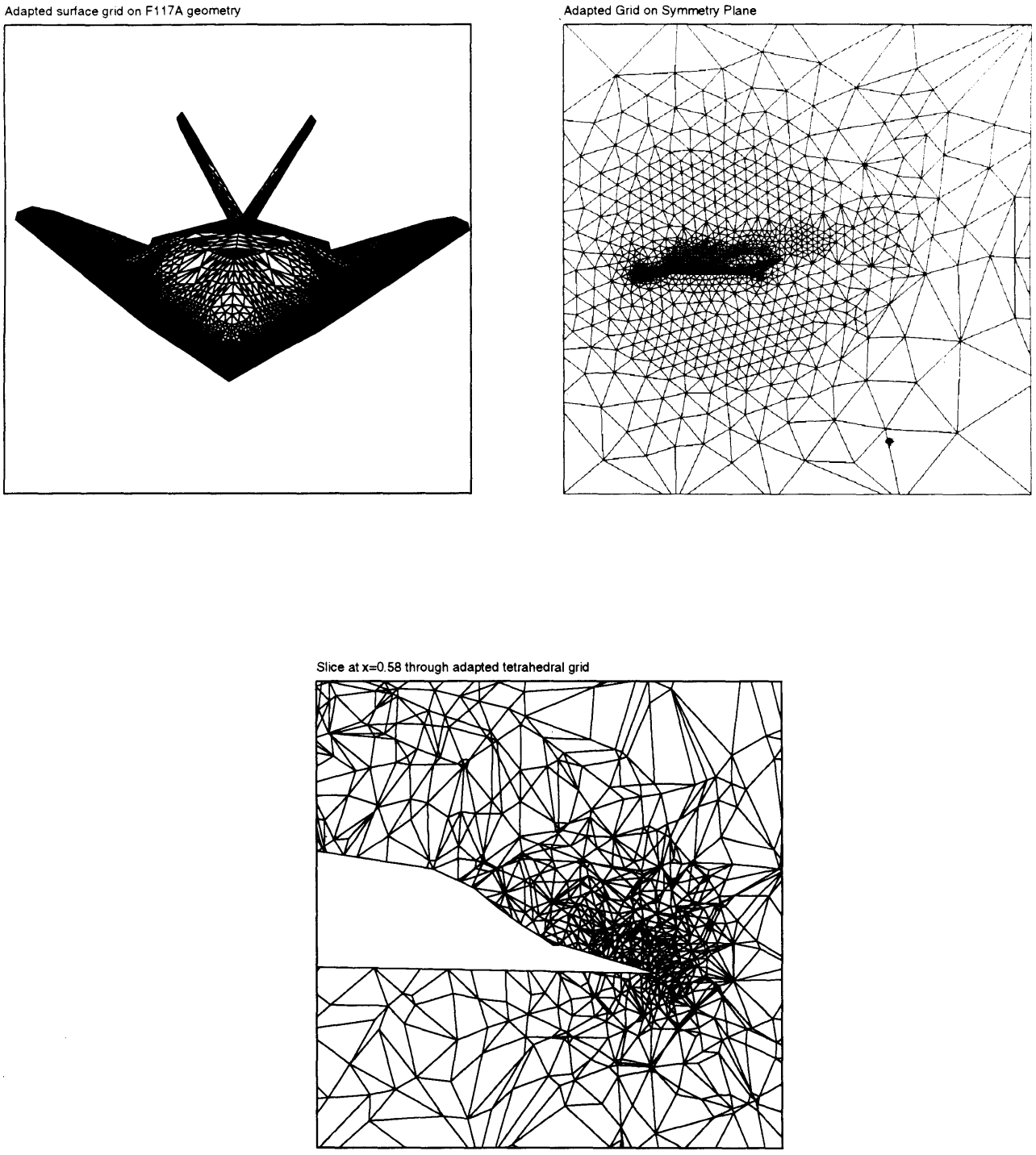

Figure 6.4: Surface grid, symmetry plane and slice for adapted grid

6.3 Results

All cases are at a free stream Mach number of 0.3. The speed was chosen in order to minimize the CPU time and the compressibility effects when comparing experimental and computational data. In the next few sections, a discussion of the lift coefficient, type of breakdown and location of breakdown will be given. Because so many data were acquired, only the interesting flow features for each of the computed cases are emphasized .

6.3.1 General Features of Solutions

Figures 6.5, 6.6 and 6.7 respectively show streamlines through the leading edge vortex for α=7, 10, 15, 20, 25 and 30 degrees and total pressure loss across contours for α=7 and 20 degrees are shown in Figure 6.8.

For α below 15 degrees, the streamlines above the wing show only a very weak, barely discernible. The streamlines appear to be almost parallel to one another which suggests a practically smooth flow over the body. For α of 15 degrees and above, the calculated results show a much stronger vortical behavior above the wing. The streamlines are twisted around one another, reflecting the local streamwise angular rotation rate or vorticity which has developed in the fluid flow. In order to illustrate this better, Figure 6.8 shows total pressure loss contours for α=7 and 20 degrees respectively. A note is made that the jagged appearance of the total pressure loss contours is introduced by the interpolation procedure in the visualization software and does not represent inaccuracies in the calculation [12]. Figure 6.9 shows a total pressure loss profile across the vortex. It is clear that total pressure loss is localized to that part of the computational domain where the vortex has formed : the loss is highest at the core and is approximately zero outside of the vortex. The contours of total pressure loss should therefore clearly show a vortex if it has formed. Again, as can be seen from Figure 6.8 the vortex at α=20 degrees is much stronger and better defined.

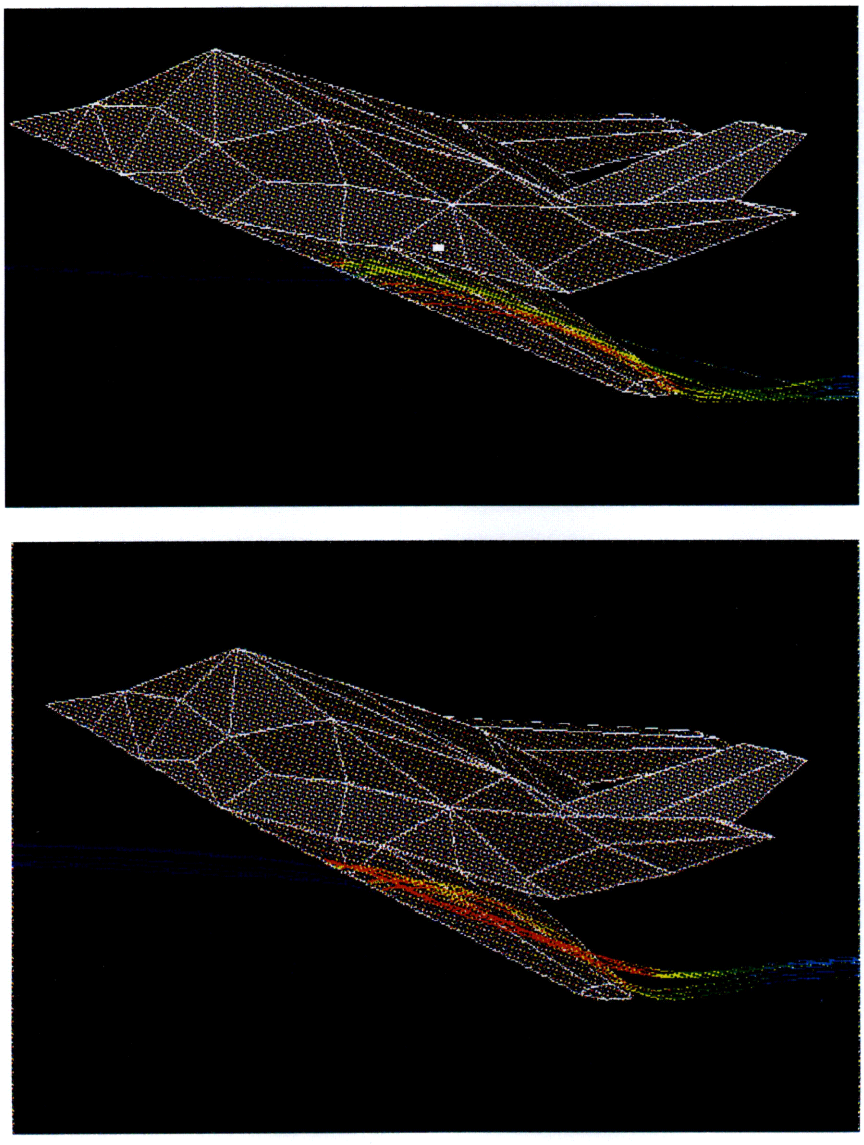

Figure 6.5 : Streamlines through vortex at 7 and 10 degrees

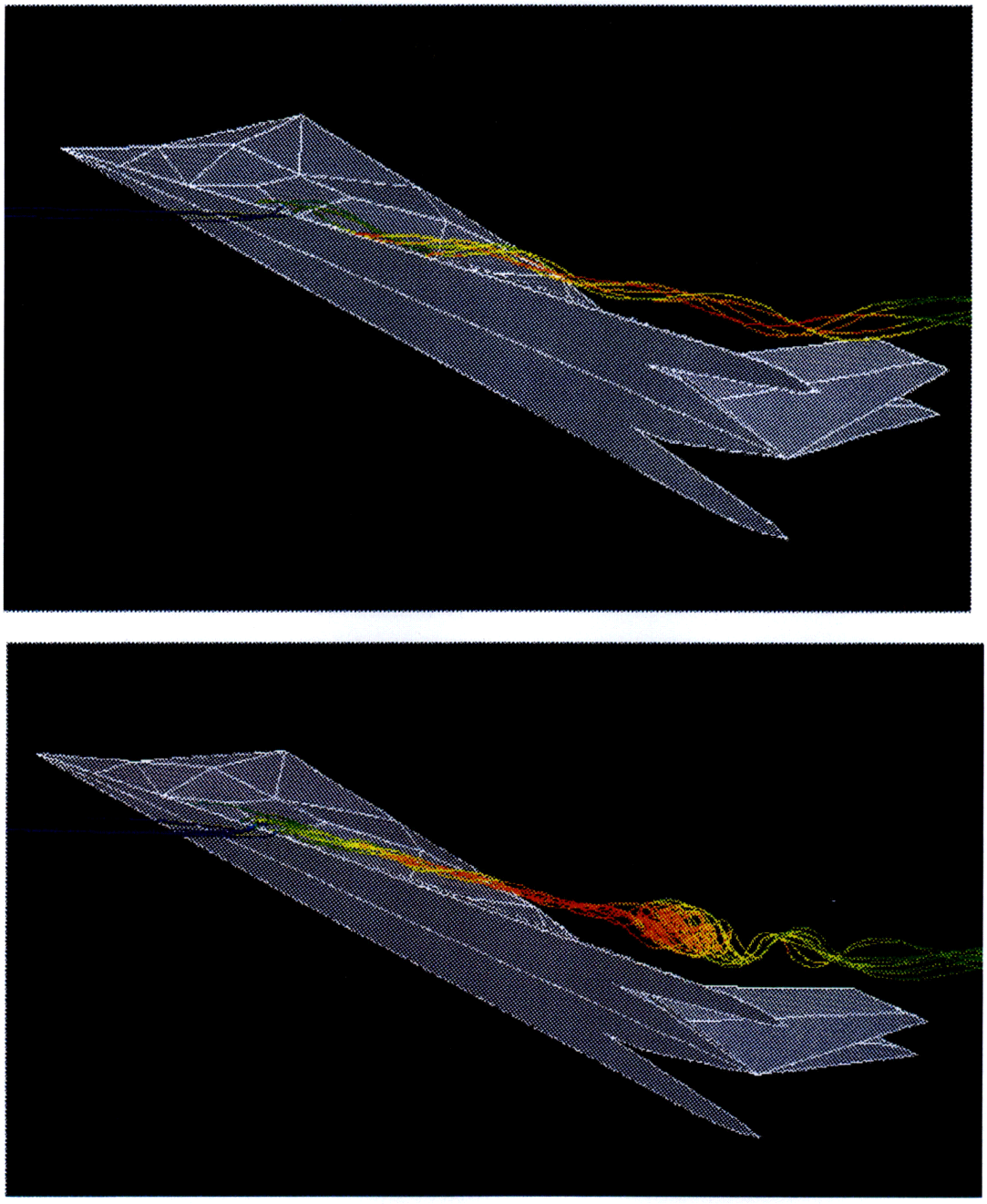

Figure 6.6 : Streamlines through vortex at 15 (top) and 20 (bottom) degrees

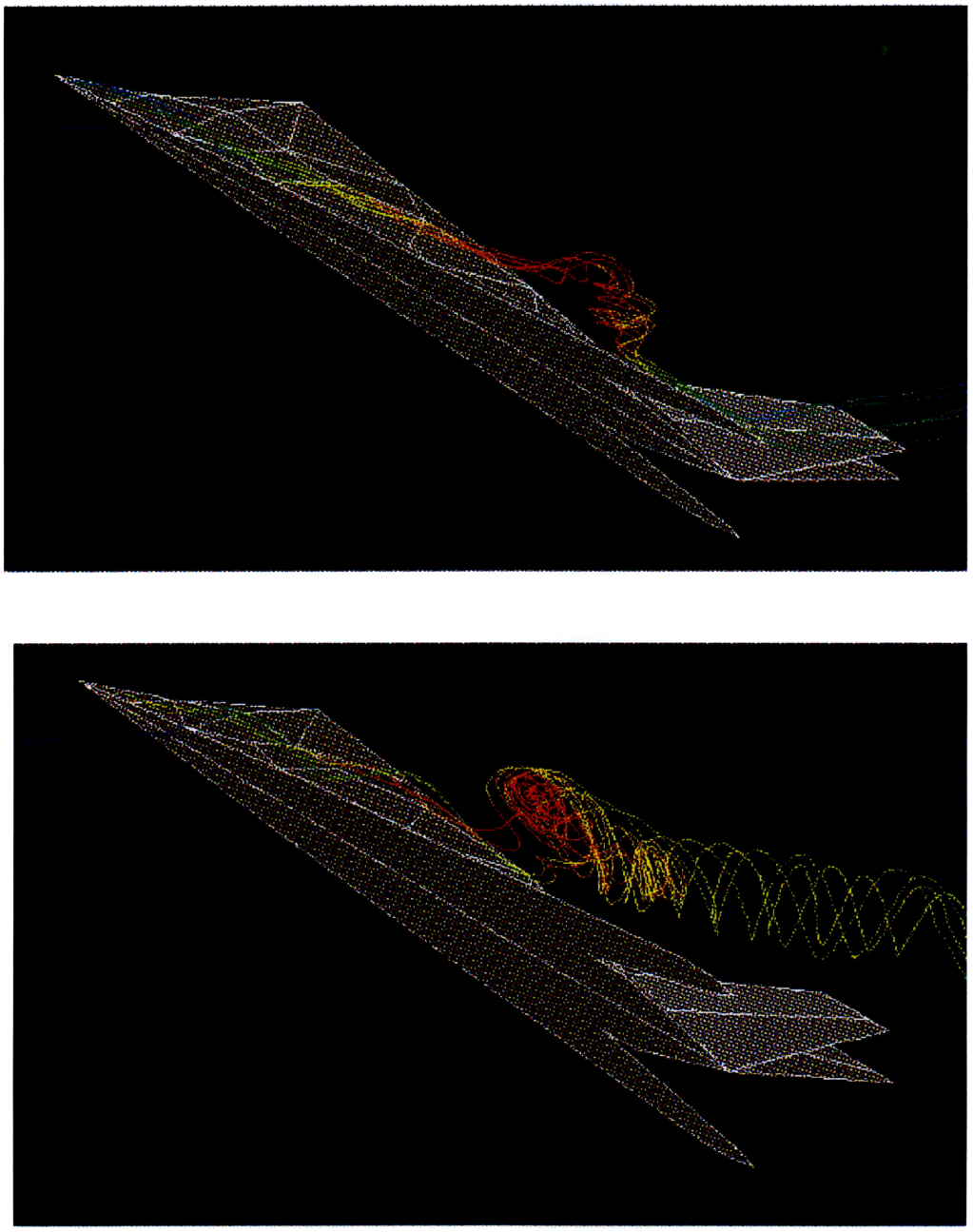

Figure 6.7 : Streamlines through vortex at 25 and 30 degrees

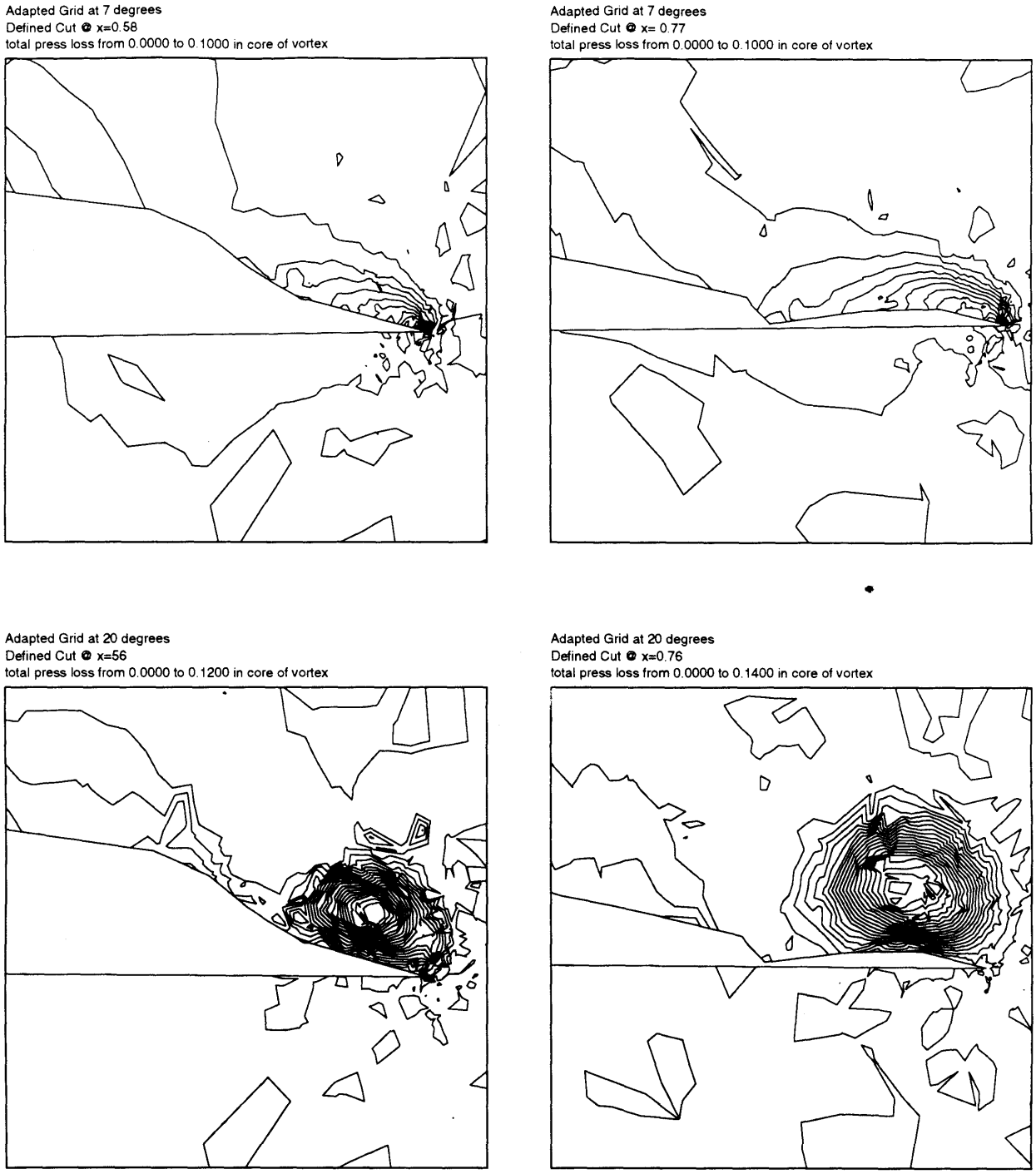

Figure 6.8: Total Pressure Loss for α=7 deg and α=20 deg

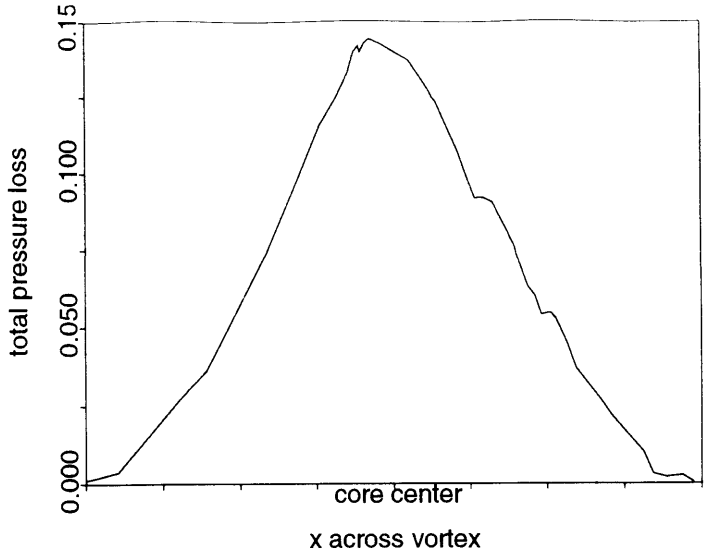

Figure 6.9: Typical total pressure loss profile across vortex

6.3.2 Vortex Breakdown : 20, 25 and 30 degrees angle of attack

For angles exceeding 15 degrees, there appears to be a sudden enlargement of the vortex core which suggests that vortex breakdown has occurred. As can be observed from the streamlines in Figure 6.6 and 6.7, breakdown clearly is of the bubble-type for α=20 degrees and the α=25 and 30 degree cases seem to show a rather spiral behavior. Figure 6.10 shows a visualization and a schematic representation of an axisymmetric or bubble vortex breakdown as found by Sarpkaya [19]. Figure 6.11 is a magnification of the breakdown region found from the computations at 20 degrees. Clearly, the structure of the breakdown is similar to the bubble found by Sarpkaya. Figure 6.12 shows two stream lines as they move through the breakdown region at α=25 degrees. A spiral type behavior is obvious. A close-up view for breakdown at α=30 degrees is presented in Figure 6.13. There appears to be a bubble followed by a spiral behavior. Breakdown has been observed by Sarpkaya as an intermediate structure in between the spiral and bubble-type breakdown [19]. Because the streamlines inside the bubble follow a path which is mostly of spiral behavior, breakdown at α=30 degrees is classified as the asymmetric spiral type in this thesis. Figure 6.14 shows surface pressure contours and streamlines through the vortex core for α=20, 25 and 30 degrees. Blue signifies the region of lowest pressure on the surface and red represents high surface pressure. The

Figure 6.10: Photograph of bubble type breakdown

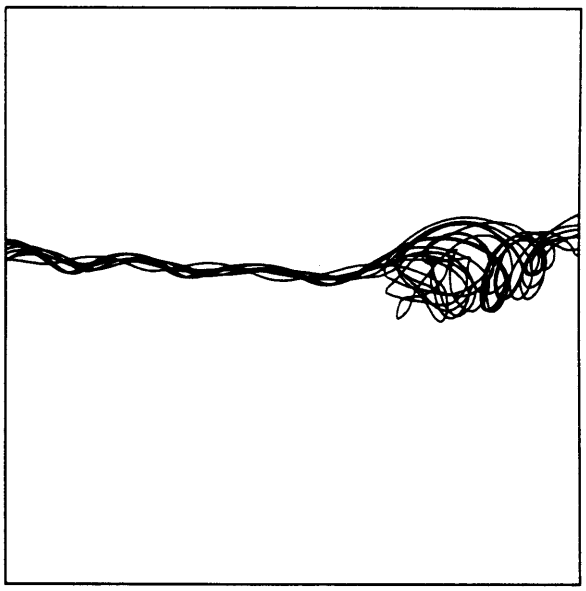

Figure 6.11: Bubble type vortex at 20 degrees

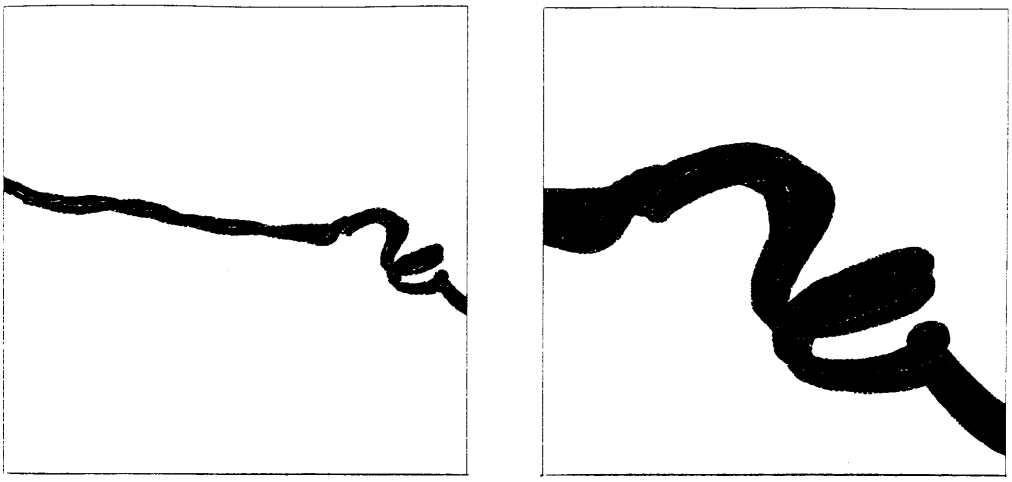

Figure 6.12: Spiral type vortex at 25 degrees

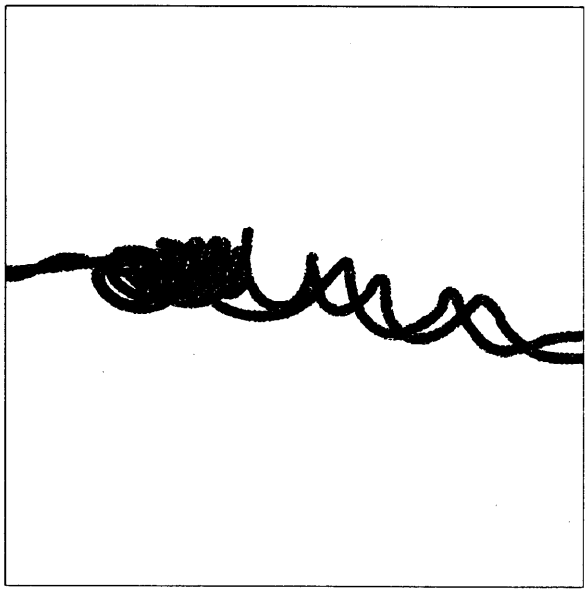

Figure 6.13: Spiral type vortex at 30 degrees

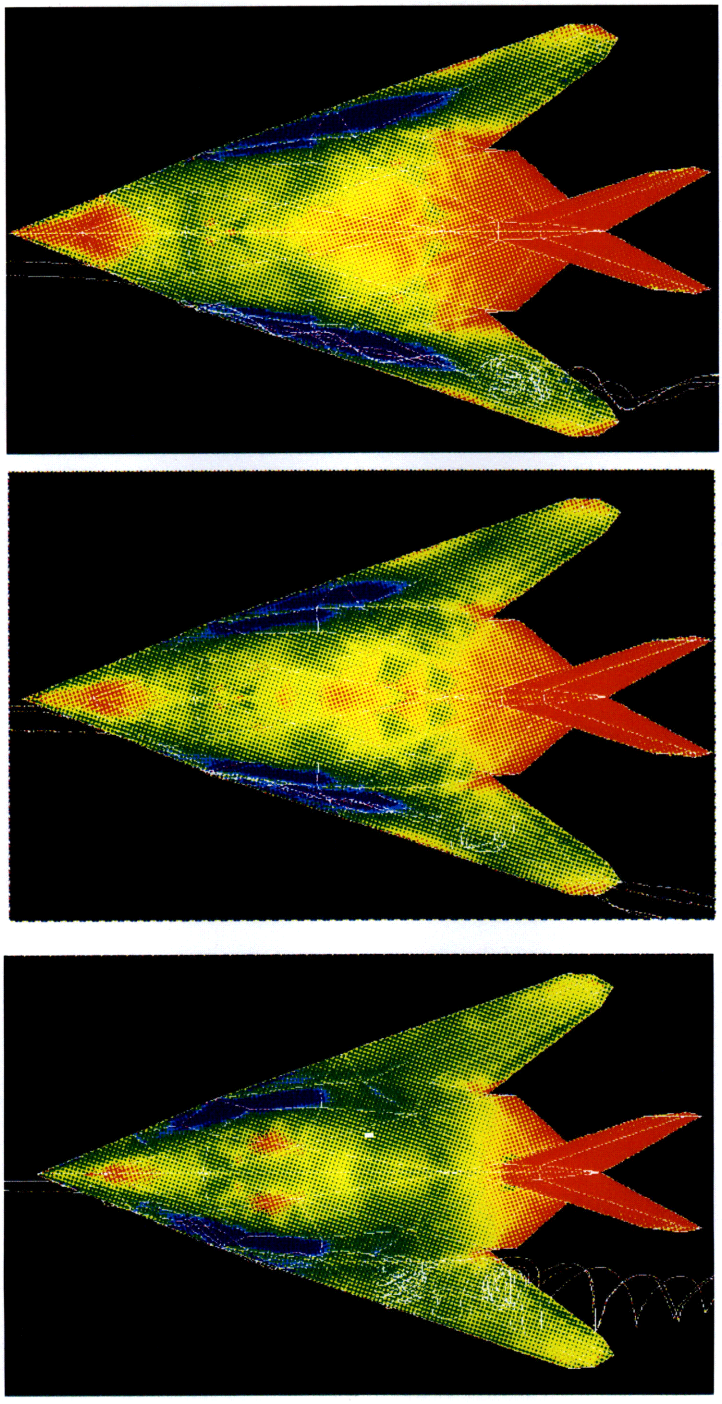

Figure 6.14 : Pressure Contours for 20(top) 25(middle) and 30(bottom) degrees

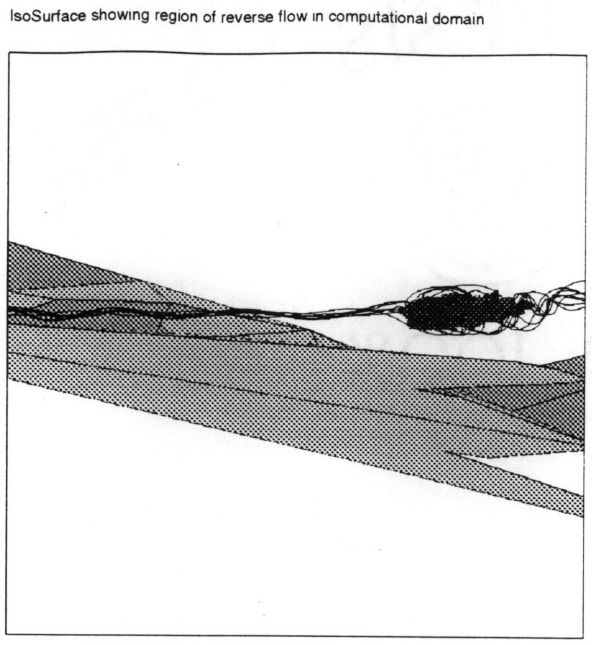

Figure 6.15: Region of reverse flow for α=20 degrees

effect of the acceleration of the flow due to the presence of the leading edge vortex can be seen by the low pressure region underneath the vortex. When no breakdown occurs, this region of low pressure is expected to stretch on the wing all along the vortex and provide high lift for the aircraft. However, for α=20, 25 and 30 degrees the low pressure region suddenly disappears where the streamlines indicate breakdown. For aircraft with a continuous leading edge, this effect of breakdown on the surface pressure increases with increasing angle of attack as the breakdown region moves upstream. This can clearly be observed from Figure 6.14 where the area of intense low surface pressure gets smaller as the angle of attack is increased. As a result, a loss of lift is expected and a decrease of nose down pitching moment occurs because vortex breakdown influences the rear part of the wing.

Figure 6.15 shows the region of reverse flow in the computational domain for α=20 degrees. The region of reverse flow is represented in gray and forms a bubble inside the burst. Upstream of the breakdown, the axial velocity is not reversed. Figure 6.16 shows the profiles of axial velocities across the vortex in front of breakdown and inside the breakdown region. The jet profile in front and the wake profile inside the burst suggest the stagnation of the vortex when breakdown occurs. The same results were verified for

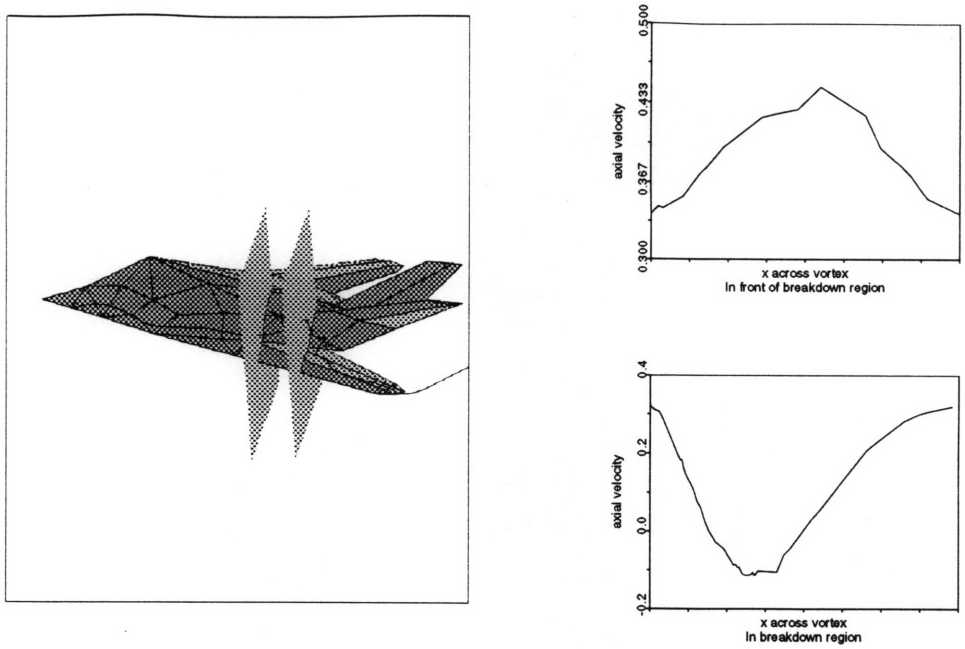

Figure 6.16: Axial velocity profiles across vortex

α=25 and 30 degrees.

6.3.3 Effect of Adaptive Refinement on Solutions

Figures 6.17 and 6.18 both show a vortex at 20 degrees on an unadapted grid (top picture) and adapted grid (bottom picture). Figure 6.17 shows several cutting planes along the F117A axis and Figure 6.18 is a close up of one cutting plane location. The contours are of total pressure loss, red being high and blue low. For both cases, the computations result in a vortex. However, the importance of adaptive refinement for the solution is clear. On the unadapted grid, the vortex is very diffused and lies right on top of the wing. When looking at the embedded grid, the total pressure loss contours show a vortex with an improvement of resolution and separated vortical flow above the wing. When looking at the streamlines, no vortex breakdown was observed at any angle of incidence on the unadapted grids while the adaptation resulted in vortex breakdown at angles of attack of 15 degrees and higher. This becomes apparent from Figure 6.19. The lift curve for both the unadapted and adapted grids is shown. For low angles of attack, when breakdown does not occur, the unadapted grid generally results in a lower lift coefficient. This agrees with the discussion in section 6.3.4. However, the observation

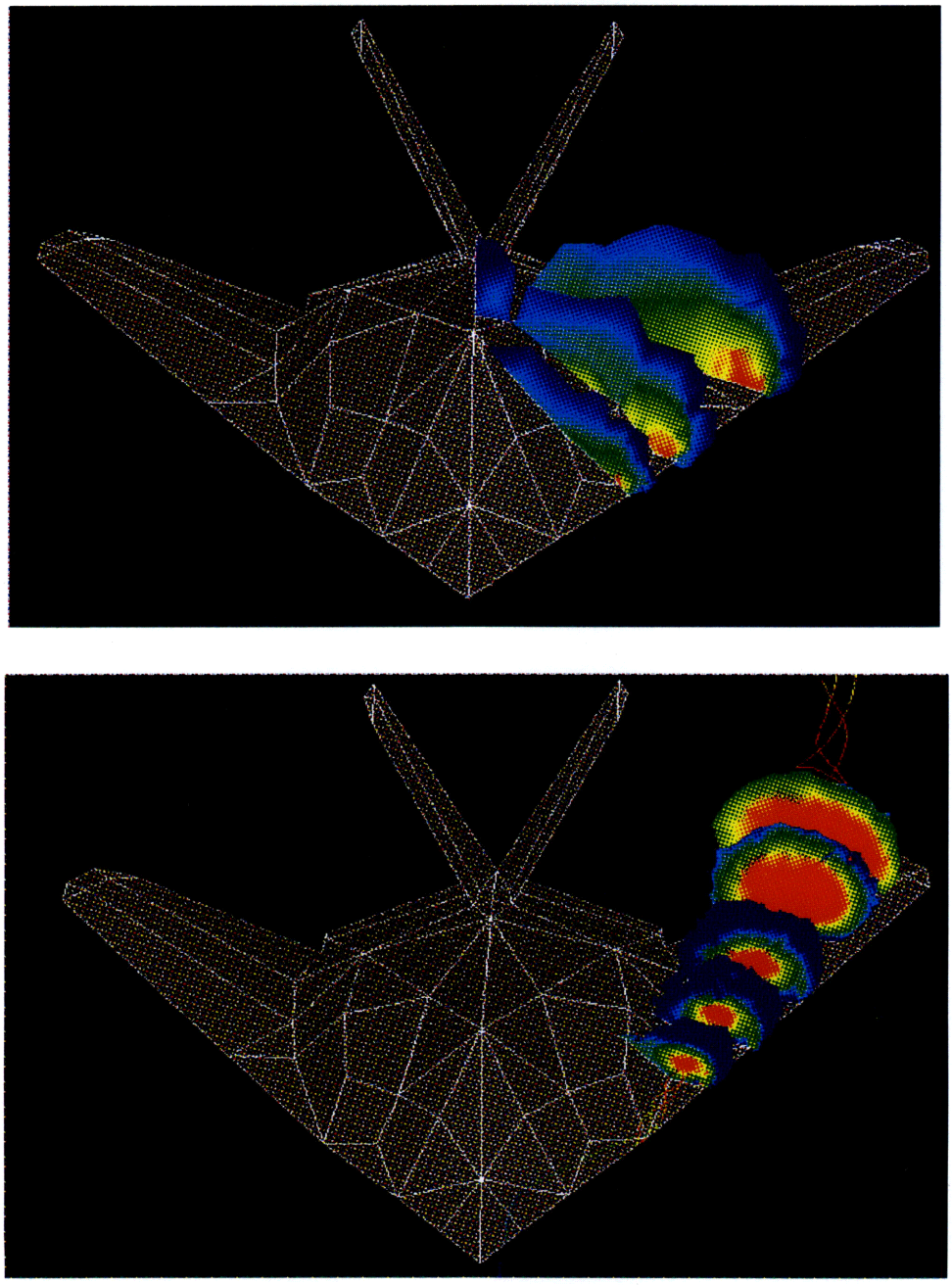

Figure 6.17 : Vortex on an unadapted(top) and adapted(bottom) grid at 20 deg

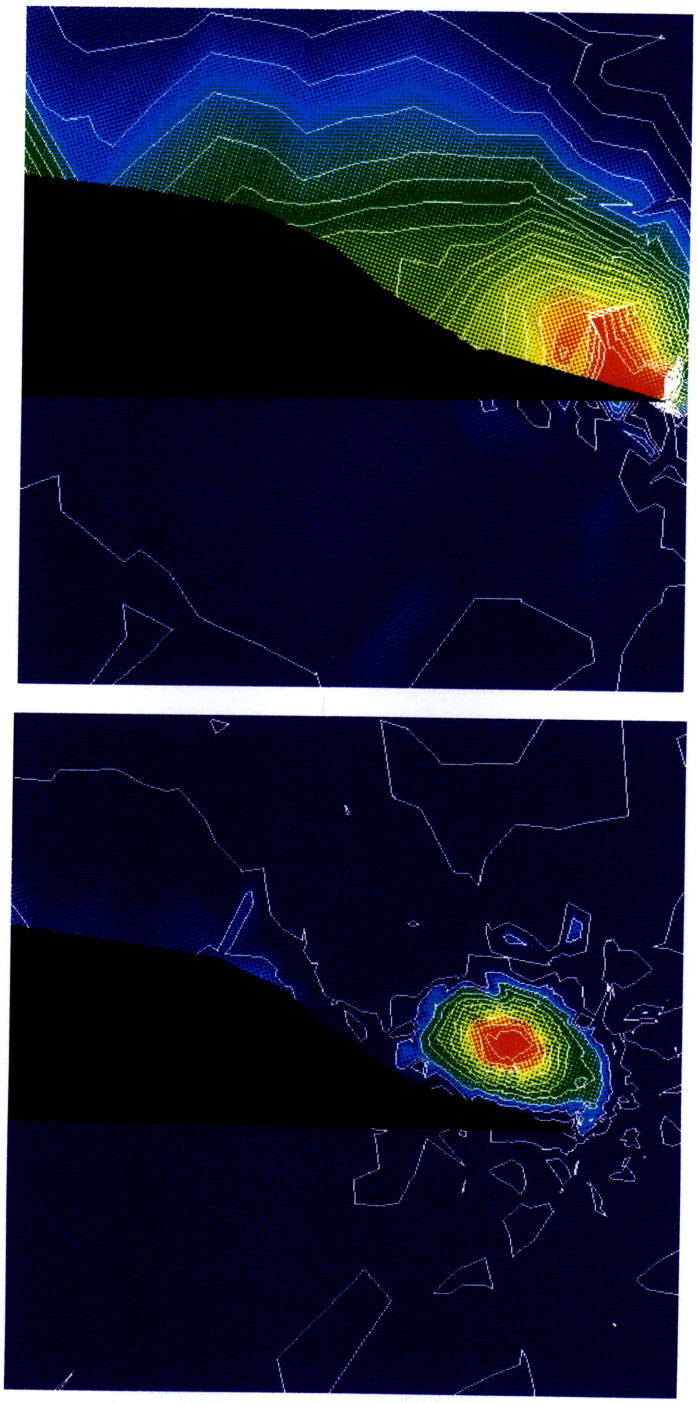

Figure 6.18 : Cutting plane through vortex on an unadapted(top) and adapted(bottom) grid at 20 deg

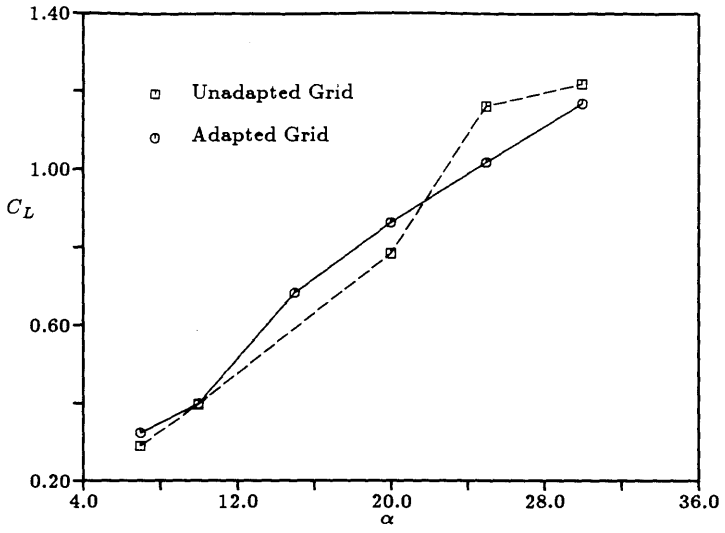

Figure 6.19: F117A C_L-α curves

is made that at angles of attack exceeding 20 degrees, where breakdown has moved a significant amount upstream, the unadapted grid over predicts lift as compared to the adapted grid. This is due to the fact that no breakdown occurs in the unadapted calculations.

6.3.4 Lift and Moment Curves

The wind tunnel is operated at 27 m/sec. This corresponds to a Reynolds number of 1.23×10^6 (based on the length of the model). Experiments were performed at other velocities and results were insensitive to Reynolds numbers in the range of 6×10^5-1.23×10^6 except at the highest angle of attack as shown in Figure 6.20. At the highest Reynolds number, the experiment was repeated, and both sets of data are shown in the subsequent plots.

Visualization in the tunnel shows an enlarged vortex core at $\alpha = 20$ and higher. This agrees very well with the computational results as described above. The angle at which

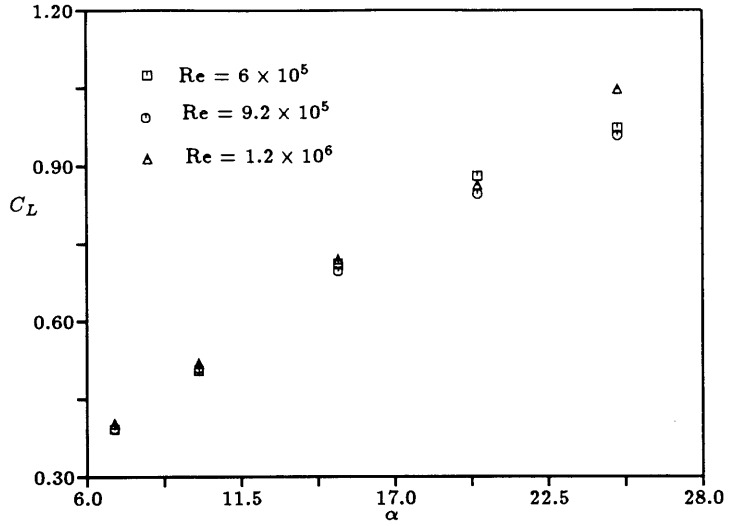

Figure 6.20: Experimental C_L-α curves for several Reynolds Numbers

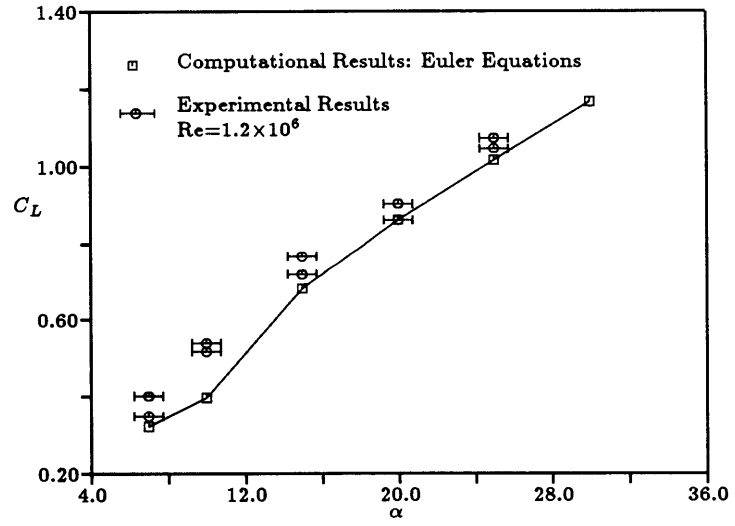

Figure 6.21: F117A C_L-α curve

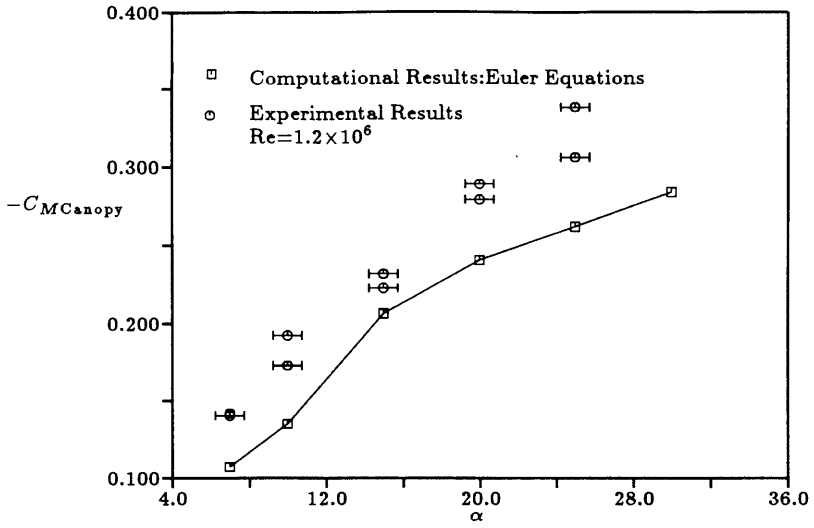

Figure 6.22: F117A C_M-α curves

vortex breakdown first occurs over the wing is also confirmed by the actual operation of the F117A. The aircraft is not allowed to fly at an angle of attack exceeding 18 degrees because of the effects of vortex breakdown [2].

Figure 6.21 shows the lift curves (C_L-α) obtained from both the calculations and experimental data. Error bars for α represent the uncertainty in setting the geometrical angle of attack. The two sets of data indicate the uncertainty in the measured lift coefficient. The general trend is that the numerical results under predict the experimental curve. The Euler solution for lift shows a very good agreement with the experimental results for α of 15 degrees and higher. In this range, the two curves are almost parallel. For α below 15 degrees, however, the experimental results are significantly higher than the numerical results. In the next few paragraphs, three reasons for the under prediction of the lift curve are discussed and two explanations for the more significant discrepancies at low angles of attack are suggested.

The overall shift of the experimental lift curve may be caused by the angular flow variation in the jet of the wind tunnel. Wind tunnels are known to exhibit an angular

variation of 0.75 degrees or even 1.0 degree [17]. It is very hard to correct the effect of angularity since the variation of flow angle may change with the tunnel speed. The tunnel used for this work has an unknown angularity. For future work, it is recommended that the measurement of the effect of angularity in the wind tunnel is done.

Another source of error could be the differences between the tested and the computed geometries. The theoretical model of the F117A was modified to simplify the generation of a grid. As described in Chapter 4, several assumptions about the geometry are made and the engine exhaust area is completely removed and replaced by a slanted plane. This could be a likely source of error.

Finally, it is possible that other vortices are present in the experiments which the calculations cannot pick up. Because of the faceted geometry of the F117A, one expects to observe more than one vortex in the flow field, for example a vortex coming off the sharp edges of the canopy. However, since the initial unadapted grid is very coarse on the main body, it is not possible to capture such a vortex without refining the initial grid. Because of storage requirements this was not done. As a result, the computed lift could be lower than the experimental results.

For angles of attack below 15 degrees, discrepancies between the computational and experimental results are more significant than for higher angles. As can be seen from the total pressure loss contours in Figure 6.8, the vortex found for 7 degrees is very weak and lies right on the wing surface all along the wing. The same vortex structure is found for the 10 degree case. For the experimental tests at 7 and 10 degrees, smoke visualization clearly showed a leading edge vortex. Two possible explanations for these differences at low angles of attack are suggested.

One possibility is that even the adapted grid is too coarse in the region where the vortex is forming and therefore is not able to resolve the vortex properly. Because the vortical behavior is very weak at low angles of attack, adaptation of the grid using entropy as the adaptation parameter is not as effective as it is for higher angles of incidence.

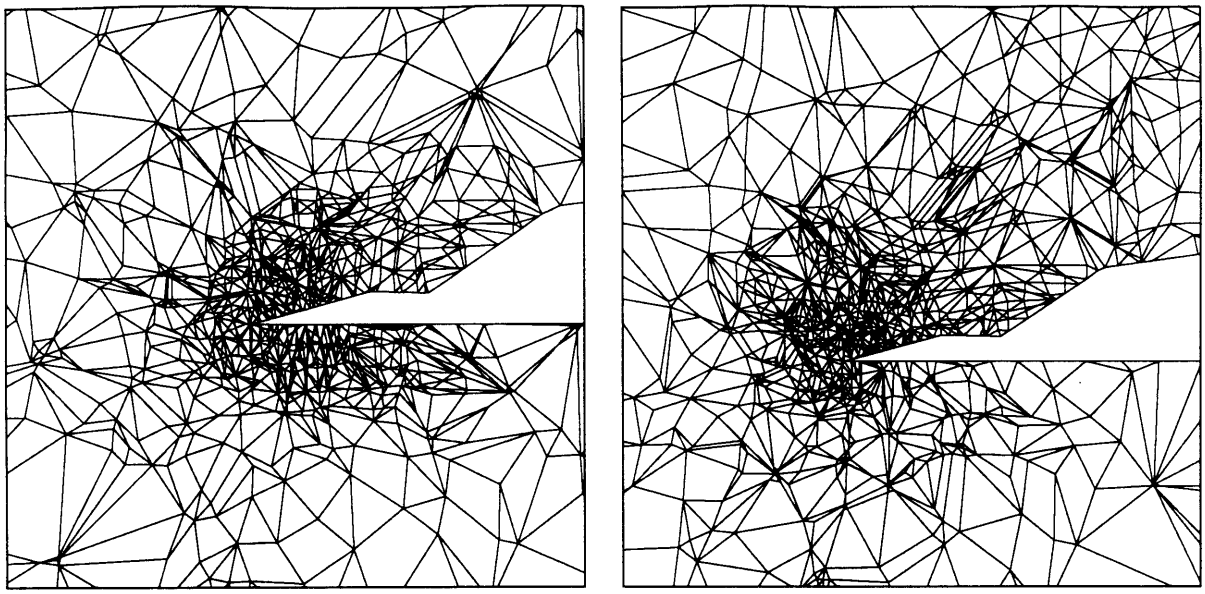

Figure 6.23: Adapted grid for 7 degrees(left) and 20 degrees(right)

As a result, new grid points are added in areas away from the vortex, and the grid is therefore still pretty coarse in the vicinity of the expected vortex. This becomes apparent when looking at Figure 6.23. The left picture shows the adapted grid at 7 degrees and the right picture shows the grid at 20 degrees. It is clear that for 7 degrees, new nodes were added in areas where no vortex is expected, for example below the F117A body. Since it is set that 30% of the nodes are adapted, the grid will be coarser above the wing. Consequently, the vortex cannot be properly captured and the lift is lower than expected. A more efficient way to cluster nodes above the wing might be to add extra sources using the grid generator FELISA instead of performing adaptation.

In order to estimate the effect of grid density on the lift curve, adaptation for 7 degrees was performed with a larger percent of the nodes to be adapted. This results in a slightly higher lift coefficient. Rizzi also found that it is a general trend with Euler codes that as a grid is refined more, pressure coefficients decrease and the lift coefficients increase [18]. Even though it is unlikely that grid density is the only source for the significant discrepancy at low angles, it is our expectation that as the grid is refined more, the lift coefficient will increase.

Another possible reason for the under prediction of lift at low angles of attack is that the Euler equations may not be an appropriate model for vortex flows at low Mach number and small angles of incidence. The boundary layer due to viscous effects which can not be modeled by the Euler equations my affect the formation of the vortex. This might be a possible reason why a vortex is clearly observed in the wind tunnel but not in the computations. It was not possible to perform viscous calculations to investigate this possibility.

As can be seen from Figure 6.21, the influence of vortex bursting on the slope of the lift curve is not very significant for both the experimental and the computational results. Kegelman and Roos found in an experimental investigation that for a delta wing of 70 degree sweep and less, the coupling between the vortex burst and lift is not strong [7]. This could also apply to the F117A since its simple planform is basically a delta wing with a sweep angle of 68 degrees.

Figure 6.22 shows the pitching moments curves for both the experimental and computational results. For simplicity, the moments are calculated around the canopy of the F117A. For the 1/32 scaled model used in the experiments, the canopy is located 15 and 5.8 centimeter behind and above the nose respectively. In the theoretical model for which the length of the body is 1, the canopy is located .3 and .12 behind and above the nose respectively.

When comparing the moment curves, it is clear that the theoretical curve under predicts the experimental curve. Possible explanations for this general trend are the same as for the lift curves. However, the discrepancies between both moment curves are more drastic than for the lift curves. This is due to the fact that the moment curve is a lot more sensitive to inaccuracies, especially in those areas where the moment is large as for example the trailing edge of the aircraft. Also, flow angularity in the wind tunnel generally affects the pitching moment tests more than lift [17]. In contradiction with the results for lift, the moment curves show a better comparison at angles of attack below 15 degrees and the discrepancy is more significant at high angles of attack. One possible

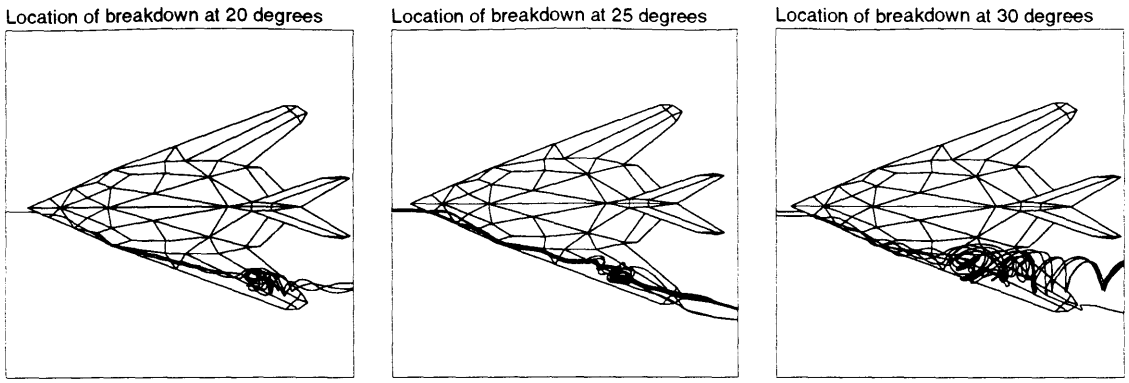

Figure 6.24: Location of Breakdown

explanation for this behavior is that the effect of the modified engine outlet area in the computational model becomes significant in determining the moment at high angles. Because the outlet is replaced by a slanted plane, separation at the trailing edge is not as likely for the computations as for the experiments. As a result, the pressure on the back end of the aircraft is higher than expected. Since the moment arm is very large there, this area of high pressure decreases the nose down pitching moment.

It is also clear that there is a drop in the slope of the computational moment curve due to vortex breakdown. In the pitching moment curve, the effect of vortex breakdown is more distinctive than for the lift curve. The same observation was made by Hummel and Srinivasan for their calculations over slender delta wings [6]. As a result of vortex breakdown, the F117A is not allowed to fly over 18 degrees because above that range, the airplane starts to assume a rapidly increasing pitch-up [2]. One can imagine that from the results as the pressure over the aft part of the wing increases as breakdown moves forward, causing a nose-up pitching moment.

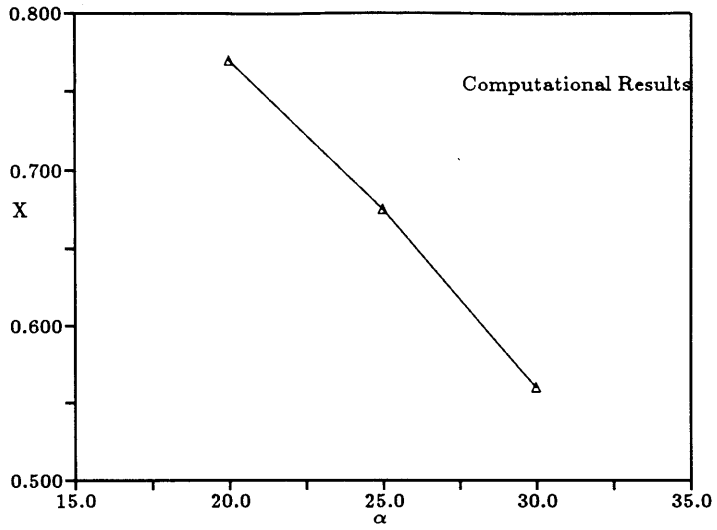

Figure 6.25: Location of breakdown

6.3.5 Location of Breakdown

Figure 6.24 shows a top view of the F117A for α=20, 25 and 30 degrees. Streamlines reflect the location of vortex breakdown in each of the pictures. It is obvious that the location of breakdown indeed depends on the angle of incidence. At low angles of attack, the breakdown is located far downstream of the aircraft and therefore, it does not appear in the calculations. As α is increased, the breakdown moves upstream and crosses the trailing edge.

Figure 6.25 shows how the breakdown location varies with α for the computational data. X is the distance from the nose and the length of the aircraft is 1. For this thesis, breakdown is defined as the point where reverse flow in the core of the vortex first occurs. As can be seen, at 20 degrees, the breakdown has crossed the trailing edge of the wing (located at X approximately 1) and lies above the wing. As the angle of incidence is increased, breakdown moves upstream and at 30 degrees, it has moved up close to the leading edge. It is our expectation that at 15 degrees, breakdown occurs right behind the trailing edge of the wing. Because the grid has not been sufficiently

refined downstream of the aircraft, it does not show up in the computations.

Chapter 7
Conclusions

The goal of the research work described in this thesis was to determine whether an adaptive finite element Euler solver on an unstructured mesh of tetrahedra has the capability to accurately resolve leading edge vortices and in particular to capture vortex breakdown at high angles of attack. The importance of these powerful solution methods was illustrated by performing a typical computational study of the flow characteristics of Lockheed's F117A stealth fighter. Wind tunnel tests were also done to compare with the computational results. Once grid generation and computations were performed, lift and moment coefficients were obtained and compared for a range of angles of attack in order to verify the solutions.

The F117A was chosen for this project for very specific reasons. The unconventional features of the F117A would suggest a complex vortical flow field. Since the Euler solver used for this work does not model the separated flow which would occur on bodies with more rounded surfaces, the F117A is very suitable for this study. At the same time, the faceted surface geometry of the F117A greatly simplifies the digitizatal definition of the model and ,therefore, allows a manual data acquisition of the spatial coordinates.

To digitize the model, a simple geometry definition of the aircraft was developed. The grid generation system created both a surface and a volume grid in the computational domain using the advancing wave front method. An Euler solver with Galerkin finite element spatial discretization and four stage Runge-Kutta time-stepping was used to perform the computations. In order to capture the important flow features, one level of adaptation based on entropy was done on the grid.

Results which reflect the capability of the solution methods used were presented. Calculations on adapted grids were done for the range of angles of attack between 7 and

30 degrees. By looking at streamlines and total pressure loss above the wing for each case, strong leading edge vortices were observed at angles of attack of 15 degrees and higher. At 7 and 10 degrees, a clear vortex is not present but a total pressure loss is observed above the wing. By determining the region of reverse flow in the vortex and by looking at surface pressure contours, vortex breakdown was found at α of 20 degrees and higher. At 20 degrees, the streamlines through the vortex core clearly showed a bubble-type breakdown. On the other hand, for 25 and 30 degrees, a spiral breakdown was observed. Visualization in the wind tunnel also showed breakdown for angles exceeding 15 degrees. This agrees with the actual limitation criteria of the F117A aircraft which is an angle of attack of 18 degrees[2].

Grid resolution was found to have a very significant effect on the accuracy of the solution. The computations for all angles of incidence showed an insufficient resolution of the vortex on the coarse grid. No vortex breakdown occurred at any angle of attack using this grid. The vortical behavior for all solutions on the coarse grid was also very weak. From the results, it is clear that the accuracy of a computed solution to the Euler equations is directly related to the number of grid points. By looking at the solutions, one may conclude that least one level of adaptation of the grid is necessary in order to capture a vortex vortex at α exceeding 15 degrees. For α below 15 degrees, a second level of adaptation might be necessary to accurately capture the weak leading edge vortex. It is our expectation that adding more grid points in the region of total pressure loss, a vortex will be captured at the lower angles. A second level of adaptation was not performed because of the storage requirements for such a computation.

The accuracy of the computations was determined by comparing the slopes of the computational and experimental lift curves. Overall, the computations showed to be consistent with the experiments. However, the computational lift curve showed a significant discrepancy with the experimental data at low angles of attack(below 15 degrees) and the moment curves at high angles of attack (above 15 degrees).

Additional studies are needed to understand whether angularity plays an important role in the under prediction of the computational lift curve to the experimental data. One way to check this would be to flip the model in the wind tunnel (in other words, test it

right side up). However, since a wire balance system was used for this project, it would not be practical to do this. A suggestion to correct angularity would be to find an average value of the angle by measuring the flow angle at several downstream stations.

This study has focussed on the performance of a finite element Euler solver with adaptive refinement on an unstructured mesh of tetrahedra. The results justify the usage of these solution methods to calculate the flow around complex three dimensional objects with sharp leading edges (to provide flow separation). The use of a mesh which is completely unstructured simplified the generation of a grid in the complex 3-D computational domain and,at the same time, allowed for grid adaptation in a straight forward manner. The flow solver also demonstrated the power of the solving Euler equations in capturing the important flow feature of vortex breakdown.

Bibliography

[1] G. Batchelor. *An Introduction to Fluid Dynamics.* Cambridge University Press, 1967.

[2] D. A. Brown. *Retired director of engineering Lockheed Corporation.* Private Communication, February 15, 1993.

[3] M. Escudier. *Vortex Breakdown : Observations and Explanations.* Prog. Aerospace Sci. Vol.25 pp.189-221, May 1987.

[4] M. Escudier and J. Keller. *Recirculation of Swirling Flow: A Manifestation of Vortex Breakdown.* AIAA J. 23(1), 111-116, 1985.

[5] R. Haimes and M. Giles. *Unstructured Finite Element Mesh Generation and Adaptive Procedures for CFD.* AGARD Specialist's Meeting, May 1989.

[6] D. Hummel and P. Srinivasan. *Vortex Breakdown Effects on the Low-Speed Aerodynamic Characteristics of Slender Delta Wings in Symmetrical Flow.* Journal of the Royal Aeronautical Society, Vol.71, July 1966.

[7] J. Kegelman and F. Roos. *Effects of Leading-Edge Shape and Vortex Burst on the Flowfield of a 70 Degree Sweep Delta-Wing.* 27th Aerospace Sciences Meeting, AIAA 89-0086, January 1989.

[8] M. Lambert. *Jane's All The World Aircraft.* 1991.

[9] N. Lambourne and D. Breyer. *The Bursting of Leading-Edge Vortices - Some Observations and Discussions of the Phenomenon.* Rep and Mem no. 3282, Aeronautical Research Council, 1962.

[10] A. Landsberg. *Adaptation for Vortex Flows Using a 3-D Finite Element Solver.* Master's thesis, Massachusetts Institute of Technology, November 1990.

[11] J. Miller. *Lockheed F-117 Stealth Fighter.* Aerofax Inc, 1991.

[12] D. Modiano. *Computation of Unsteady Flow Around a Pitching Delta Wing.* PhD thesis, Massachusetts Institute of Technology, December 1992.

[13] R. Newsome and A. Kandil. *Vortical Flow Aerodynamics-Physical Aspects and Numerical Simulation.* AIAA 87-0205, January 1987.

[14] J. Peraire and K. Morgan. *DRAFT : Lisa User Manual.* Unpublished note, November 1991.

[15] J. Peraire, K. Morgan, and J. Peiro. *VISUAL3: Interactive Unsteady Unstructured 3D Visualizatrion.* AIAA Paper 91-0794, January 1991.

[16] E. Polhamus. *Prediction of Voftex-Lift Characteristics Based on a Leading-Edge Suction Analogy.* AIAA Paper 69-113, October 1963.

[17] A. Pope and J. Harper. *Low-Speed Wind Tunnel Testing.* John Wiley and Sons, Inc.,New York, Sidney, London, 1966.

[18] I. Rizzi. *3-D solutions to Euler equations with one million grid points.* AIAA 23(12), December 1985.

[19] T. Sarpkaya. *On Stationary and Travelling Vortex Breakdowns.* Journal of Fluid Mechanics, 45:545-559, 1971.

[20] G. Strang. *Introduction to Applied Mathematics.* Wellesley-Cambridge Press, 1986.

Appendix A

Calculation of Matrices for Spatial Discretization

The integration of Equations 3.14 - 3.17 is carried out in the local coordinate system (ξ_1, ξ_2, ξ_3) of natural coordinates, as defined in section 3.2.2. The spatial derivatives of the interpolation functions are evaluated by a projection onto the new coordinate system. The chain rule is used and the following are obtained :

$$\frac{\partial N_i}{\partial x} = \frac{\partial N_i}{\partial \xi_1}\frac{\partial \xi_1}{\partial x} + \frac{\partial N_i}{\partial \xi_2}\frac{\partial \xi_2}{\partial x} + \frac{\partial N_i}{\partial \xi_3}\frac{\partial \xi_3}{\partial x} \tag{A.1}$$

$$\frac{\partial N_i}{\partial y} = \frac{\partial N_i}{\partial \xi_1}\frac{\partial \xi_1}{\partial y} + \frac{\partial N_i}{\partial \xi_2}\frac{\partial \xi_2}{\partial y} + \frac{\partial N_i}{\partial \xi_3}\frac{\partial \xi_3}{\partial y} \tag{A.2}$$

$$\frac{\partial N_i}{\partial z} = \frac{\partial N_i}{\partial \xi_1}\frac{\partial \xi_1}{\partial z} + \frac{\partial N_i}{\partial \xi_2}\frac{\partial \xi_2}{\partial z} + \frac{\partial N_i}{\partial \xi_3}\frac{\partial \xi_3}{\partial z} \tag{A.3}$$

The interpolation functions for spatial discretization were chosen by Modiano as follows as described in section 3.2.2:

$$\begin{aligned} N_1 &= \xi_1 \\ N_2 &= \xi_2 \\ N_3 &= \xi_3 \\ N_4 &= \xi_4 = 1 - \xi_1 - \xi_2 - \xi_3 \end{aligned} \tag{A.4}$$

This was a good choice since :

$$\begin{aligned} \partial N_1/\partial \xi_1 = 1 \quad & \partial N_1/\partial \xi_2 = 0 \quad & \partial N_1/\partial \xi_3 = 0 \\ \partial N_2/\partial \xi_1 = 0 \quad & \partial N_2/\partial \xi_2 = 1 \quad & \partial N_1/\partial \xi_3 = 0 \\ \partial N_3/\partial \xi_1 = 0 \quad & \partial N_3/\partial \xi_2 = 0 \quad & \partial N_3/\partial \xi_3 = 1 \\ \partial N_4/\partial \xi_1 = -1 \quad & \partial N_4/\partial \xi_2 = -1 \quad & \partial N_4/\partial \xi_3 = -1. \end{aligned} \tag{A.5}$$

When combining the equations above the following is obtained :

$$\begin{aligned} \frac{\partial N_1}{\partial x} &= \frac{\partial \xi_1}{\partial x} & \frac{\partial N_1}{\partial y} &= \frac{\partial \xi_1}{\partial y} & \frac{\partial N_1}{\partial z} &= \frac{\partial \xi_1}{\partial z} \\ \frac{\partial N_2}{\partial x} &= \frac{\partial \xi_2}{\partial x} & \frac{\partial N_2}{\partial y} &= \frac{\partial \xi_2}{\partial y} & \frac{\partial N_2}{\partial z} &= \frac{\partial \xi_2}{\partial z} \\ \frac{\partial N_3}{\partial x} &= \frac{\partial \xi_3}{\partial x} & \frac{\partial N_3}{\partial y} &= \frac{\partial \xi_3}{\partial y} & \frac{\partial N_3}{\partial z} &= \frac{\partial \xi_3}{\partial z} \\ \frac{\partial N_4}{\partial x} &= -\frac{\partial \xi_1}{\partial x} - \frac{\partial \xi_2}{\partial x} - \frac{\partial \xi_3}{\partial x} & \frac{\partial N_4}{\partial y} &= -\frac{\partial \xi_1}{\partial y} - \frac{\partial \xi_2}{\partial y} - \frac{\partial \xi_3}{\partial y} & \frac{\partial N_4}{\partial z} &= -\frac{\partial \xi_1}{\partial z} - \frac{\partial \xi_2}{\partial z} - \frac{\partial \xi_3}{\partial z}. \end{aligned} \tag{A.6}$$

In order to evaluate the spatial derivatives of the volume coordinates in the previous equation, the spatial coordinates are evaluated as the state quantitiesdescribed in Chapter 3, i.e. via interpolation between the nodes, so that :

$$x^C(\xi_1, \xi_2, \xi_3) = x_i N_i^C(\xi_1, \xi_2, \xi_3) = x_1\xi_1 + x_2\xi_2 + x_3\xi_3 + x_4(1 - \xi_1 - \xi_2 - \xi_3) \tag{A.7}$$

$$y^C(\xi_1, \xi_2, \xi_3) = y_i N_i^C(\xi_1, \xi_2, \xi_3) = y_1\xi_1 + y_2\xi_2 + y_3\xi_3 + y_4(1 - \xi_1 - \xi_2 - \xi_3) \tag{A.8}$$

$$z^C(\xi_1, \xi_2, \xi_3) = z_i N_i^C(\xi_1, \xi_2, \xi_3) = z_1\xi_1 + z_2\xi_2 + z_3\xi_3 + z_4(1 - \xi_1 - \xi_2 - \xi_3). \tag{A.9}$$

In order to calculate the Jacobian from Equations A.7- A.9, a more indepth discussion of the mesh geometry is needed. Figure A.1 shows the a tetrahedral cell. The outward-pointing area normal to each cell face is constructed by taking the cross product of two edge vectors of the face. The only requirement is that it points outward.

Using this method and referring to Figure A.1,

$$\vec{S_1} = \frac{1}{2}(\vec{x}_{32} \times \vec{x}_{42})$$

$$\vec{S_2} = \frac{1}{2}(\vec{x}_{41} \times \vec{x}_{31})$$

$$\vec{S_3} = \frac{1}{2}(\vec{x}_{21} \times \vec{x}_{41})$$

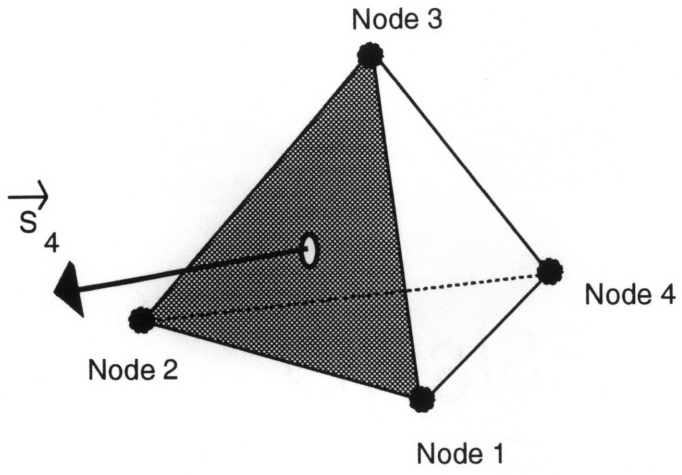

Figure A.1: Tetrahedral Cell Nomenclature

$$\vec{S_4} = \frac{1}{2}(\vec{x}_{31} \times \vec{x}_{21}) \tag{A.10}$$

where x_{ij}=x_i-x_j, y_{ij}=y_i-y_j and z_{ij}=z_i-z_j and where $\vec{x}_{ij} = \vec{x}_i - \vec{x}_j$ is the edge vector between the ith and jth nodes of the terahedron as shown in Figure A.1.

The volume of a tetrahedral cell is :

$$V^C = \frac{1}{6}\begin{vmatrix} x_{21} & y_{21} & z_{21} \\ x_{31} & y_{31} & z_{31} \\ x_{41} & y_{41} & z_{41} \end{vmatrix} \tag{A.11}$$

$$= \frac{1}{6}(x_{21}y_{31}z_{41} + y_{21}z_{31}x_{41} + z_{21}x_{31}y_{41} \tag{A.12}$$

$$-z_{21}y_{31}x_{41} - x_{21}z_{31}y_{41} - y_{21}x_{31}z_{41} \tag{A.13}$$

The Jacobian matrix of the coordinate transformation can now be calculated.

$$J = \frac{\partial(x,y,z)}{\partial(\xi_1,\xi_2,\xi_3)}$$

$$= \begin{bmatrix} x_{14} & x_{24} & x_{34} \\ y_{14} & y_{24} & y_{34} \\ z_{14} & z_{24} & z_{34} \end{bmatrix} \tag{A.14}$$

Inverting this Jacobian matrix :

$$J^{-1} = \frac{\partial(\xi_1, \xi_2, \xi_3)}{\partial(x, y, z)}$$

$$= \frac{1}{|J|} \begin{bmatrix} y_{24}z_{34} - z_{24}y_{34} & z_{24}x_{34} - x_{24}z_{34} & x_{24}y_{34} - y_{24}x_{34} \\ z_{14}y_{34} - y_{14}z_{34} & x_{14}z_{34} - z_{14}x_{34} & y_{14}x_{34} - x_{14}y_{34} \\ y_{14}z_{24} - z_{14}y_{24} & z_{14}x_{24} - x_{14}z_{24} & x_{14}y_{24} - y_{14}x_{24} \end{bmatrix} \quad \text{(A.15)}$$

by using Equation A.13, the inverse Jacobian can be rewritten :

$$J^{-1} = -\frac{1}{3V^C} \begin{bmatrix} S_{x1} & S_{y1} & S_{z1} \\ S_{x2} & S_{y2} & S_{z2} \\ S_{x3} & S_{y3} & S_{z3} \end{bmatrix} \quad \text{(A.16)}$$

where V^C is the volume of the cell, and S_{xj},S_{yj} and S_{zj} are the Cartesian components of the area vector of the jth face. The final step can now be satisfied by substituting Equation A.16 into Equation A.6.

$$\begin{array}{lllllll} \frac{\partial N_1}{\partial x} = -\frac{S_{x1}}{3V^C} & \frac{\partial N_1}{\partial y} = -\frac{S_{y1}}{3V^C} & \frac{\partial N_1}{\partial z} = -\frac{S_{z1}}{3V^C} \\ \frac{\partial N_2}{\partial x} = -\frac{S_{x2}}{3V^C} & \frac{\partial N_2}{\partial y} = -\frac{S_{y2}}{3V^C} & \frac{\partial N_2}{\partial z} = -\frac{S_{z2}}{3V^C} \\ \frac{\partial N_3}{\partial x} = -\frac{S_{x3}}{3V^C} & \frac{\partial N_3}{\partial y} = -\frac{S_{y3}}{3V^C} & \frac{\partial N_3}{\partial z} = -\frac{S_{z2}}{3V^C} \\ \frac{\partial N_4}{\partial x} = \frac{S_{x1}+S_{x2}+S_{x3}}{3V^C} & \frac{\partial N_4}{\partial y} = \frac{S_{y1}+S_{y2}+S_{y3}}{3V^C} & \frac{\partial N_4}{\partial z} = \frac{S_{z1}+S_{z2}+S_{z3}}{3V^C} \\ = -\frac{S_{x4}}{3V^C} & = -\frac{S_{y4}}{3V^C} & = -\frac{S_{z4}}{3V^C}. \end{array} \quad \text{(A.17)}$$

Using these definitions, the transformation and evaluation of the mass and residual matrices is straightforward [12].